A robust DG-ALE formulation for nonlinear shallow water interactions with a partially immersed object

Ali Haidar, Fabien Marche, Francois Vilar

A robust DG-ALE formulation for nonlinear shallow water interactions with a partially immersed object

Ali Haidar[a,*], Fabien Marche[a], Francois Vilar[a]

[a] *IMAG, Univ Montpellier, CNRS, Montpellier, France*

Abstract

We introduce a new numerical strategy designed for the modelization and simulation of nonlinear interactions between surface waves in shallow water and a stationary partially immersed surface piercing object. At the continuous level, the flow domain is globally modeled with the nonlinear hyperbolic shallow-water equations, while the description of the flow beneath the object reduces to a nonlinear ordinary differential equation. The coupling between the flow and the object is formulated as a free-boundary problem, associated with the computation of the time evolution of the spatial locations of the air-water-object interface. At the discrete level, the proposed formulation relies on an arbitrary-order discontinuous Galerkin approximation, which is stabilized with a recent *a posteriori* Local Subcell Correction method. The time evolution of the air-water-object interface is computed from an Arbitrary-Lagrangian-Eulerian description and a suitable smooth mapping between the initial frame and the current configuration. For any order of polynomial approximation, the resulting global approximation algorithm is shown to: (i) preserve the Discrete Geometric Conservation Law, (ii) ensure the preservation of the water height positivity at the sub-cell level, (iii) preserve the class of motionless steady states (well-balancing), possibly with the occurrence of a partially immersed object. Several numerical computations, involving solitary waves and bores propagations and transformations over varying topographies and/or in the vicinity of the object, highlight that the proposed numerical model: (i) effectively allows to model the flow-object interactions and provides the time-evolution of the air-water-object contact points, (ii) is able to accurately handle strong flow singularities without any robustness issues, (iii) retains the highly accurate sub-cell resolution of discontinuous Galerkin schemes.

Keywords: nonlinear shallow water, discontinuous Galerkin, *a posteriori* local sub-cell correction, Arbitrary-Lagrangian-Eulerian, wave-object interactions

1. Introduction

The mathematical and numerical study of the propagation and transformations of surface waves in the presence of a floating structure is a complex problem in which one has to model the time evolution of a mechanical system made of a solid object which is partially immersed in an incompressible fluid. Besides the hydrodynamic issues generally associated with the simulation of nonlinear free-surface flows, an important additional difficulty is that the immersed part of the structure, called the *wetted surface* in what follows, generally depends on time, leading to an additional free-boundary

*Corresponding author

Email addresses: ali.haidar@umontpellier.fr (Ali Haidar), fabien.marche@umontpellier.fr (Fabien Marche), francois.vilar@umontpellier.fr (Francois Vilar)

problem. The modelization of such a system can be traced back to the pioneering work [19], in which a linear potential model is used for the hydrodynamics (the fluid is assumed irrotational and inviscid), and the motion of the solid is assumed to be of small amplitude around a steady mean position. Although being over-simplified for applications of interest, this approach put the light on the important and difficult issue of defining suitable transmission conditions between the *exterior* area (where the surface waves do not interact with the structure) and the *interior* area (the fluid under the solid, applying a pressure on the wetted surface). Such a linear strategy has been refined, extended and adapted in several subsequent studies: let mention for instance the important application domains of offshore structures [26], floating Wave Energy Converters (WEC) [23] or floating breakwaters, see for instance [34, 21]. When combined with Boundary Element Methods (generally a linear-BEM applied in the frequency domain) for the computation of the hydrodynamics, the linear potential theory still defines the background of several popular dedicated software. Indeed, linear models are particularly fast, especially when compared to Reynolds Averaged Navier-Stokes (RANS) simulations (see for instance [36] for an application to WEC) or to potential approaches with a nonlinear surface boundary condition. Moreover, for small to moderate sea states, the assumptions related to linear theory generally provide numerical previsions with reliable leading orders of approximation.

However, for larger sea states, nonlinear effects may become overriding. Hence, several attempts to account for nonlinear effects have been reported in the literature and most of them rely on fully nonlinear potential flow models used together with nonlinear BEM, in time/physical domain, also allowing to account for varying bathymetry [13]. Another strategy, yet far less investigated, is to use some simplified asymptotic nonlinear models instead of the full water-waves equations and this may appear as an interesting compromise between linear models and CFD strategies. Depth-integrated models may be used at least to describe the free-surface fluid evolution, like in [20] where floating breakwater are modelized using a Boussinesq-type (BT) model and a Finite-Difference (FD) scheme. The flow under the breakwater is regarded as a confined flow and the pressure field beneath the floating structure is determined by solving implicitly the Laplace elliptic equation. But asymptotic flow models may be also used to describe the flow beneath the floating structure, see for instance [4] where the Kadomtsev-Petviashvili (KP) equations are used to compute wave generation by ships in shallow water, or [17, 35, 18] where some BT equations also model the interactions in the near-ship flows. Let also mention the recent numerical study [2], in which a BT model computes the heave (vertical) motion of objects with straight-sided boundaries, which are assumed vertical at the fluid-structure contact line in order to avoid the update of the contact points location.

Recently, a new formulation of the fully nonlinear floating object problem has been introduced in [22], describing the flow with respect to the free-surface elevation and the horizontal depth-integrated discharge instead of the velocity potential, with a particular emphasize put on the elliptic equation solved by the pressure of the fluid on the underside of the partially immersed object. Specifically focusing on the hyperbolic Nonlinear Shallow Water (NSW) equations, some Initial Boundary Value Problems (IBVP) are analyzed in [16], for the horizontal surface dimension $d = 1$. In particular, a general theory for a class of quasi-linear hyperbolic IBVP with a free-boundary is introduced, and applied to the coupling between the NSW equations and a partially immersed object, providing a firm mathematical background to the numerical study proposed in the present work.

Indeed, the NSW equations of [6] are one of the most widely used set of equations for simulating long wave hydrodynamics. Considering their hydrostatic and hyperbolic nature, in comparison to the dispersive nature of more sophisticated models such as the BT models, the NSW equations generally provide an accurate representation of steep-fronted flows, such as dam-breaks, flood waves or

bores propagation. There are however very few studies concerning possible extensions of the NSW equations to incorporate partly immersed objects. Let mention for instance the very recent studies [9, 10] for the computation of congested shallow water flows with a compressible/incompressible projection scheme, or again [2] as the dispersive effects of the chosen BT equations are actually neglected in the vicinity of the floating structure, hence locally reducing to the NSW equations.
Indeed, the study of a fluid with freely moving boundaries is a difficult problem, involved in several engineering domains like aeroelasticity or fluid-structure interactions. From a numerical viewpoint, in order to avoid interface-tracking methods, one requires the formulation to handle moving domains in a robust way, while ensuring the needed accuracy and conservation properties. Additionally, the interactions of flows with moving boundaries may also result in additional unsteady phenomena, coming with the need of high-order accurate approximations to resolve the unsteadiness of flows at various scales.
In such a context, the Arbitrary Lagrangian-Eulerian (ALE) description is a popular choice for several flow problems involving time-varying boundaries. Initially developed within some Finite-Difference (FD) methods in [15], and later extended to Finite-Element (FE) and Finite-Volume (FV) methods for both fluids and structures, see for instance [7] for a review, the ALE method is generally put forward as combining the best of both Lagrangian and Eulerian worlds: the computational mesh can move with an arbitrary velocity, which may be chosen independently from the material velocity. This provides a welcome flexibility in handling moving computational domains, avoiding the issues usually associated with the tracking of interfaces in the purely Eulerian approaches, as well as the large distortions generally encountered in the pure Lagrangian framework, when larger time evolutions and spatial motions are considered.
Besides the issue of handling moving meshes, reaching an optimal (possibly high-) order of accuracy where the solution is smooth is also a major concern in the design of discrete formulations for such problems and the development of high-order methods for solving real-world problems is a broad and very active research topic in computational physics. In this context, discontinuous Galerkin (DG) methods have encountered considerable improvements in recent years. They are now widely used in several large classes of problems, in fluid dynamics, geophysical flows, aero-acoustics or electromagnetism. We refer the reader to the review [5] for more details and references concerning the various applications of DG methods to flow problems. It is known that DG methods successfully combine features and capabilities coming from both FE methods and FV methods, accounting for the underlying physical processes. Among the acknowledged assets of DG methods, let mention the arbitrary-order of accuracy in space through high-order polynomials within mesh elements, the compact stencils (in comparison with high-order FV methods), the compliance towards complex geometries and general unstructured / non-conforming meshes or h/p-adaptivity. DG methods with an ALE description for moving boundaries problems in fluid-structure interactions or free-surface flows have also been considered for instance in [32, 25, 27], or in the (closely related) *space-time* DG methods of [31, 30]. Let also mention the recent Residual Distribution (RD) formulation in ALE description for the NSW on the sphere proposed in [1].
In the present work, we focus on a class of free-boundary hyperbolic problems arising in the study of nonlinear surface wave-structure interactions, and for which the evolution of the free-boundary is governed by a singular equation. Specifically, we aim at designing a robust and accurate DG discrete formulation, with an underlying ALE description of the motions which is directly modeled from the class of IBVP introduced and analyzed in [16]. This provides a new way of simulating adaptive and time-varying solutions for partially immersed structures in nonlinear shallow water flows with varying topography. As any arbitrary regular-shaped object may be considered, the wet-

ted surface and contact points locations are expected to evolve over time, and the computational grid is expected to move accordingly. To achieve this, a smooth and explicit mapping between the initial (time-independent) reference configuration and the current (time-varying) configuration is introduced, borrowed from the analysis of the continuous problem provided in [16]. The NSW equations are then recast in the reference domain, with the introduction of additional geometric terms related to the grid's motion, before being approximated through some high-order DG polynomial approximations.

Of course, it is well-known that the solution of nonlinear hyperbolic equations may encounter some loss of regularity in finite time and high-order DG methods usually suffer from the lack of nonlinear stability, as they may produce spurious oscillations in the vicinity of the solution's singularities (discontinuities but also steeply varying gradients or dry-areas for fee surface flows). To alleviate such a limitation, a stabilization strategy has to be added in order to enforce the required robustness properties, and the development of such stabilization methods is still an active field of research. Let mention [5] for the description of a widely used slope-limiter strategy for high-order DG methods applied to hyperbolic problems. However, the use of limiters in DG methods may prevent from converging towards steady-states and may also negatively impact the overall accuracy of the computation. Very recently in [14], we design and equip an arbitrary-order DG approximation for the NSW equations with an *a posteriori* Local Sub-cell Correction (LSC) method, which relies on some lowest-order corrected interface fluxes operating on a dedicated sub-partition, adapted from the general stabilization strategy for hyperbolic conservation laws developed in [33]. This method is proved to be extremely robust, while retaining the accuracy of the high-order polynomial description of the flow variables and coming with appealing sub-mesh resolution capabilities.

Hence, another objective of this paper is therefore to extend the stabilization operator of [14] to the proposed DG-ALE framework and enforce some nonlinear stability and monotonicity minimal requirements to the high-order approximations of nonlinear flows with a floating object. This stabilization procedure through corrected fluxes also comes with some suitable local conservative variables reconstructions borrowed from [24], and a definition of the Lax-Friedrichs interface flux suitable for moving meshes, rigorously ensuring that robustness and well-balancing (for motionless steady states) are embedded properties of the targeted limit lowest-order scheme. Within ALE simulations of flow problems with moving boundaries, it is also important to ensure that a numerical scheme reproduces exactly any constant solution. The Geometric Conservation Law (GCL) is a relation between the ALE mapping's Jacobian and the mesh velocity, stating that a uniform flow should not be influenced by any arbitrary grid's motion. The notion of GCL was first introduced in [29] and is also discussed for instance in [25, 27] and [12] where relations between GCL and time stability are investigated. It is also demonstrated that the global stabilized DG-ALE formulation proposed in this paper naturally ensures such a property, both at the semi-discrete level (GCL) and the fully discrete level with the Discrete GCL (DGCL), hence successfully combining well-balancing with geometric conservation. The proposed modelization and approximation strategies are then applied and validated through several test-cases involving solitary waves and bores interactions with a stationary and partially immersed object. The position of the object is specified and does not vary over time. This obviously leads to a simpler model in the interior domain, but we emphasize that even within this simplified configuration, the wetted surface and the locations of the air-water-object contact points may vary with respect to time, due to changes in the flow configuration coming from the exterior domain. This study also paves the way towards more elaborated coupling models, allowing to incorporate a floating object that may move over time.

The remainder of this paper is structured as follows. In the next section, we introduce the governing

models, based on the NSW equations for the fluid description, both for the exterior and interior domain and the coupling between the NSW equations and a stationary and partially immersed object is stated. The discrete setting, as well as the numerical discretization in space and time, are described in §3. In particular, we discuss the ALE description and the corresponding mapping, the stabilization and robustness enforcement through the *a posteriori* LSC method and exploiting the fact that the proposed DG-ALE formulation can be regarded as a FV-like scheme on a sub-mesh with particular high-order interface fluxes, as done in [14]. The resulting ability of the stabilized DG-ALE setting to preserve the well-balancing property, as well as the DGCL, are also investigated. In §4, we show several numerical assessments of the global algorithm, involving nonlinear waves run-up and reflections over objects with elliptic boundaries.

2. Modelization

In this section, we state a general description of the fluid-structure interactions problem based on the NSW equations, in the particular case $d = 1$. This model is then particularized for the case of a stationary (time-independent) and partly immersed object. Finally, an IBVP is stated from [16], as a firm mathematical basis for the next section devoted to numerical approximation.

2.1. Free-surface flow in shallow water

Given a smooth parameterization of the topography $b : \mathbb{R} \to \mathbb{R}$, denoting by H the water height, by $\eta := H + b$ the free-surface elevation, by u the horizontal (depth-averaged) velocity and by $q := Hu$ the horizontal discharge (see Fig.1), the NSW equations may be written as follows:

$$\partial_t \mathbf{v} + \partial_x \mathbf{F}(\mathbf{v}, b) = \mathbf{B}(\mathbf{v}, b'), \tag{1}$$

where $\mathbf{v} : \mathbb{R} \times \mathbb{R}_+ \to \Theta$ gathers the flow's conservative variables and is assumed to take values in the convex and open set Θ defined as

$$\Theta := \{\mathbf{v} := (\eta, q) \in \mathbb{R}^2,\ H \geq 0\}, \tag{2}$$

$\mathbf{F} : \Theta \times \mathbb{R} \to \mathbb{R}^2$ is the (nonlinear) flux function and $\mathbf{B} : \Theta \times \mathbb{R} \to \mathbb{R}^2$ is the topography source term, defined as follows:

$$\mathbf{F}(\mathbf{v}, b) := \begin{pmatrix} q \\ uq + \frac{1}{2}\mathrm{g}\eta(\eta - 2\,b) \end{pmatrix}, \quad \mathbf{B}(\mathbf{v}, b') := \begin{pmatrix} 0 \\ -\mathrm{g}\,\eta\,b' \end{pmatrix}. \tag{3}$$

The benefits of using this pre-balanced formulation instead of the classical form are highlighted in [24, 8] and also briefly recalled in the next section.

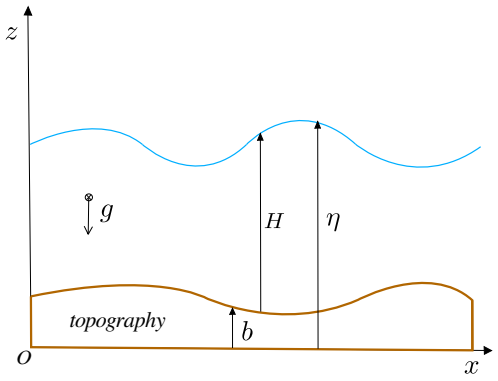

Figure 1: Free-surface flows: main notations

2.2. Free-surface shallow water flow with a partly immersed object

We consider the previous free-surface flow model and incorporate a partially immersed object on the water surface, under the assumption that there are only two contact points where the water, the air, and the object meet, see Fig. 2. We also assume that overhanging waves do not occur. For any given time value $t \geq 0$, the horizontal spatial coordinate of these contact points are denoted by $\chi_-(t)$ and $\chi_+(t)$, with $\chi_-(t) < \chi_+(t)$. Let split the horizontal line into two time-dependent sub-domains, namely the *interior* sub-domain, denoted by $\mathcal{I}(t)$, and the *exterior* sub-domain $\mathcal{E}(t)$, $\mathcal{E}(t)$ and $\mathcal{I}(t)$ being the projections on the horizontal line of the areas where the water surface get in touch with the partially immersed object and the air:

$$\mathcal{I}(t) := \left]\chi_-(t),\, \chi_+(t)\right[, \quad \mathcal{E}(t) := \mathcal{E}^-(t) \cup \mathcal{E}^+(t), \quad \mathcal{E}^-(t) := \left]-\infty,\, \chi_-(t)\right[, \quad \mathcal{E}^+(t) := \left]\chi_+(t),\, +\infty\right[, \quad (4)$$

The vectors of conservative variables respectively in $\mathcal{E}(t)$ and $\mathcal{I}(t)$ are denoted by $\mathbf{v}^{\mathrm{e}}(x,t)$ and $\mathbf{v}^{\mathrm{i}}(x,t)$ with

$$\mathbf{v}^{\mathrm{e}} := \begin{pmatrix} \eta^e \\ q^e \end{pmatrix}, \qquad \mathbf{v}^{\mathrm{i}} := \begin{pmatrix} \eta^i \\ q^i \end{pmatrix}, \quad (5)$$

and the corresponding water heights are defined by

$$H^e(x,t) := \eta^e(x,t) - b(x), \quad H^i(x,t) := \eta^i(x,t) - b(x).$$

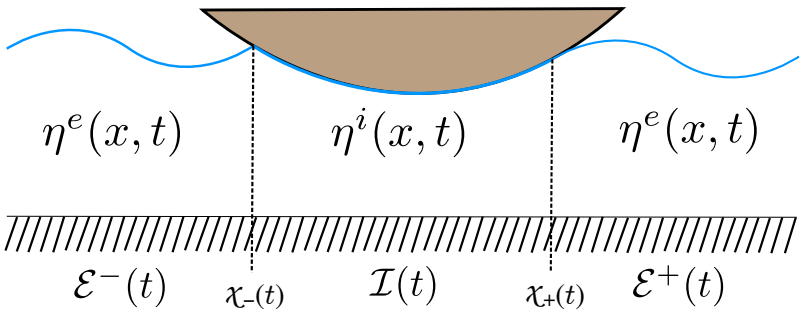

Figure 2: Shallow water interacting with a partially immersed object.

Let $\underline{\mathrm{p}}^i(x,t)$ be the pressure of the water at the underside of the object. The pressure field in the whole domain is assumed to be hydrostatic:

$$\mathrm{p}(x,z,t) := \begin{cases} \mathrm{p_{atm}} - \rho \mathrm{g}(z - \eta^e(x,t)) & \text{in} \quad \mathcal{E}(t), \\ \\ \underline{\mathrm{p}}^i(x,t) - \rho \mathrm{g}(z - \eta^i(x,t)) & \text{in} \quad \mathcal{I}(t), \end{cases} \tag{6}$$

where ρ is the density of the water and $\mathrm{p_{atm}}$ the atmospheric pressure. Thus, the general shallow water model with a partly immersed object reads as follows:

$$\begin{cases} \mathcal{E}(t) = \left]-\infty,\, \chi_-(t)\right[\cup \left]\chi_+(t),\, +\infty\right[\quad \text{and} \quad \mathcal{I}(t) = \left]\chi_-(t), \chi_+(t)\right[, & \text{(7a)} \\ \\ \left.\begin{array}{l} \partial_t \eta^e + \partial_x q^e = 0, \\ \partial_t q^e + \partial_x \Big(u^e q^e + \dfrac{1}{2} \mathrm{g} \eta^e (\eta^e - 2b) \Big) = -\mathrm{g} \eta^e b', \end{array} \right\} \quad \text{in} \quad \mathcal{E}(t) & \text{(7b)} \\ \\ \left.\begin{array}{l} \partial_t \eta^i + \partial_x q^i = 0, \\ \partial_t q^i + \partial_x \Big(u^i q^i + \dfrac{1}{2} \mathrm{g} (H^i)^2 \Big) = -\mathrm{g} H^i b' - \frac{1}{\rho} H^i \partial_x \underline{\mathrm{p}}^i, \end{array} \right\} \quad \text{in} \quad \mathcal{I}(t) & \text{(7c)} \\ \\ \eta^e = \eta^i, \quad q^e = q^i \quad \text{and} \quad \underline{\mathrm{p}}^i = \mathrm{p_{atm}} \quad \text{at} \quad \chi_\pm(t) & \text{(7d)} \end{cases}$$

In what follows, for any regular enough function $v(\cdot,t)$ defined on $\mathcal{I}(t)$, we introduce the following jump operator over the interior sub-domain:

$$[\![v]\!]_{\mathcal{I}(t)} := v(\chi_+(t),t) - v(\chi_-(t),t).$$

2.3. Free-surface shallow water flow with a stationary partly immersed object

Assuming that the object is stationary, the profile η^i on the underside of the structure is prescribed by the parameterization of the object's profile and does not explicitly depend on time (though it implicitly depends on time as $\mathcal{I}(t)$ does):

$$\eta^i(x,t) := \eta_{\mathrm{lid}}(x) \quad \text{on} \quad \mathcal{I}(t) \subset \mathcal{I}_{\mathrm{lid}}, \tag{8}$$

where η_{lid} is a given function defined on $\mathcal{I}_{\mathrm{lid}}$, which is the open interval where the parameterization of the object's underside is defined, see Fig. 3. Thus, the continuity equation in $\mathcal{I}(t)$ in (7) yields $\partial_x q^i = 0$ and therefore $q^i(x,t) = \underline{q^i}(t)$. Injecting this into the momentum equation for the interior sub-domain in (7), we obtain:

$$\frac{1}{H_i} \frac{\mathrm{d}\, \underline{q^i}}{\mathrm{dt}} + \partial_x \Big(\frac{1}{2} \big(\frac{\underline{q^i}}{H^i} \big)^2 + \mathrm{g} H^i \Big) = -\mathrm{g} b' - \frac{1}{\rho} \partial_x \underline{\mathrm{p}}^i,$$

so that $\underline{\mathrm{p}}^i$ satisfies the following Boundary Value Problem (BVP):

$$\begin{cases} \partial_x \underline{\mathrm{p}}^i = -\rho \left(\dfrac{1}{H_i} \dfrac{\mathrm{d}\, \underline{q^i}}{\mathrm{dt}} + \partial_x \big(\dfrac{1}{2} \Big(\dfrac{\underline{q^i}}{H^i} \Big)^2 + \mathrm{g} \eta^i \big) \right) & \text{in} \quad \mathcal{I}(t), & \text{(9a)} \\ \\ \underline{\mathrm{p}}^i \quad = \mathrm{p_{atm}} & \text{on} \quad \mathcal{E}(t) \cap \mathcal{I}(t). & \text{(9b)} \end{cases}$$

Integrating (9a) on $\mathcal{I}(t)$, we get:

$$\frac{\mathrm{d}\,\underline{q}^i}{\mathrm{d}t} = -\Big(\int_{\mathcal{I}(t)} \frac{1}{H^i}\,\mathrm{d}x\Big)^{-1} \Big[\!\Big[\frac{1}{2}\Big(\frac{\underline{q}^i}{H^i}\Big)^2 + \mathrm{g}\eta^i\Big]\!\Big]_{\mathcal{I}(t)}. \tag{10}$$

As a consequence, in the particular case of free-surface shallow water flows with a stationary partially immersed object, the general model (7) may be simplified as follows:

$$\begin{cases} \mathcal{E}(t) = \,]\!-\!\infty,\, \chi_{\text{-}}(t)[\,\cup\,]\chi_{+}(t),\, +\infty[\qquad \text{and} \qquad \mathcal{I}(t) = \,]\chi_{\text{-}}(t), \chi_{+}(t)[, & \text{(11a)} \\ \partial_t \mathbf{v}^{\mathrm{e}} + \partial_x \mathbf{F}(\mathbf{v}^{\mathrm{e}}, b) = \mathbf{B}(\mathbf{v}^{\mathrm{e}}, b') \qquad \text{in} \quad \mathcal{E}(t), & \text{(11b)} \\ \left.\begin{array}{rcl} \eta^i & = & \eta_{\mathrm{lid}}, \\ \dfrac{\mathrm{d}\,\underline{q}^i}{\mathrm{d}t} & = & -\Big(\displaystyle\int_{\mathcal{I}(t)} \frac{1}{H^i}\,\mathrm{d}x\Big)^{-1} \Big[\!\Big[\frac{1}{2}\Big(\frac{\underline{q}^i}{H^i}\Big)^2 + \mathrm{g}\eta^i\Big]\!\Big]_{\mathcal{I}(t)}, \end{array}\right\} \quad \text{in} \quad \mathcal{I}(t), & \text{(11c)} \\ \eta^e = \eta^i \qquad \text{and} \qquad q^e = q^i \qquad \text{at} \quad \chi_{\pm}(t). & \text{(11d)} \end{cases}$$

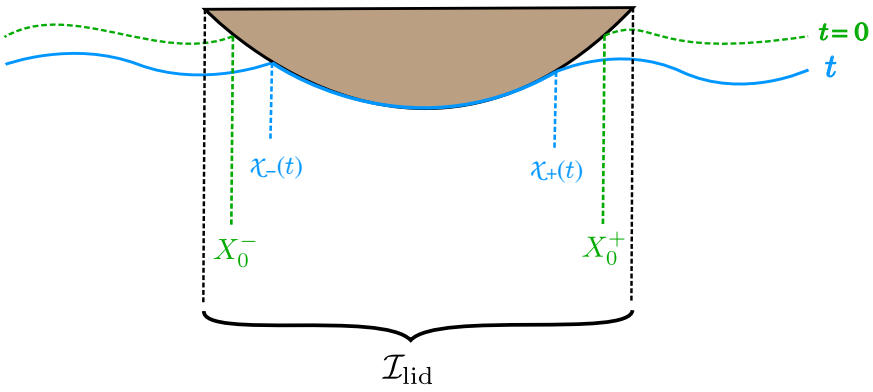

Figure 3: Water interacting with a partially immersed object.

2.4. An IBVP for the stationary object problem

Let consider the initial partition of the computational domain: $\Omega_0 := \mathcal{E}_0 \cup \mathcal{I}_0$ with

$$\mathcal{I}_0 := \,]X_0^-\,,\, X_0^+[, \quad \mathcal{E}_0 := \mathcal{E}_0^- \cup \mathcal{E}_0^+, \quad \text{with} \quad \mathcal{E}_0^- := \,]\!-\!\infty,\, X_0^-[, \quad \mathcal{E}_0^+ := \,]X_0^+,\, +\infty[, \tag{12}$$

where $X_0^{\pm}$ are the initial locations of the contact points, see Fig. 3. Supplementing (11) with the following initial data:

$$\begin{cases} \mathbf{v}^{\mathrm{e}}_{|t=0} & := \mathbf{v}^{\mathrm{e}}_0 \in H^s(\mathcal{E}_0)^2, & \text{(13a)} \\ (\chi_{\text{-}}, \chi_{\text{+}})_{|t=0} & := (X_0^-, X_0^+), & \text{(13b)} \\ \eta^i_{|t=0} & := \eta_{\mathrm{lid}} \in \mathcal{C}^1(\mathcal{I}_0), & \text{(13c)} \\ \underline{q}^i_{|t=0} & := q_0^i, & \text{(13d)} \end{cases}$$

where $H^s(\mathcal{E})$ is the Sobolev space of functions $v \in L^2(\mathcal{E})$ such that their weak derivatives up to order s have a finite L^2-norm, a local well-posedness result is stated in [16] for the particular model of shallow water flow with a stationary object, with additional assumptions on the data which aim at ensuring that: (i) no dry-state occurs in the vicinity of the object, (ii) the flow is initially sub-critical at the free boundaries, (iii) the first-order spatial derivative of the free-surface is singular at the contact points:

$$\eta_0^{\mathrm{e}\prime} - \eta'_{\mathrm{lid}} \neq 0 \qquad \text{at} \quad X_0^{\pm}, \tag{14}$$

and (iv) η_{lid} and its weak derivatives up to order s are uniformly bounded, then there exists a maximum time $T_{\max}$ and a unique solution of (11) such that $\mathbf{v}^{\mathrm{e}} \circ \chi \in \mathcal{C}^0\left([0, T_{\max}]; H^s(\mathcal{E}_0)\right) \cap \mathcal{C}^1\left([0, T_{\max}]; H^{s-1}(\mathcal{E}_0)\right)$, $\underline{q} \in H^{s+1}(0, T_{\max})$, $(\chi_{\text{-}}, \chi_{\text{+}}) \in (H^s(0, T_{\max}))^2$, where the smooth mapping χ, applying from the initial domain $\mathcal{E}_0$ to the current one $\mathcal{E}(t)$, is defined in (28).

Remark 1. In the next section, as for the numerical validations of §4, we consider the coupled problem (11) on bounded computational domains of the form

$$\Omega_t := \mathcal{E}^-(t) \cup \mathcal{I}(t) \cup \mathcal{E}^+(t) := \left]x_{\mathrm{left}},\, \chi_{\text{-}}(t)\right[\cup \left]\chi_{\text{-}}(t),\, \chi_{\text{+}}(t)\right[\cup \left]\chi_{\text{+}}(t),\, x_{\mathrm{right}}\right[,$$

so that the exterior domain's boundary is defined as $\partial\Omega := \{x_{\mathrm{left}}, x_{\mathrm{right}}\}$ and (11) has to be supplemented both with the initial data (13) and some prescribed boundary conditions on $\mathbf{v}^{\mathrm{e}}_{|x_{\mathrm{left}}}$ and/or $\mathbf{v}^{\mathrm{e}}_{|x_{\mathrm{right}}}$ depending on the flow regime, see also Remark 10.

3. Discrete formulations

3.1. Discrete setting for DG-ALE on mesh elements and FV-ALE on sub-cells

Computational domain, sub-domains and mesh

We consider an open bounded computational domain $\Omega_t := \left]x_{\mathrm{left}}, x_{\mathrm{right}}\right[$, with boundary $\partial\Omega := \{x_{\mathrm{left}}, x_{\mathrm{right}}\}$ and for any time value $t \in [0, T_{\max}]$, we introduce a partition $\mathcal{P}_\Omega(t) := \{\mathcal{E}^-(t), \mathcal{I}(t), \mathcal{E}^+(t)\}$ of Ω into disjoint sub-domains, defined through the knowledge of the *contact points* $\chi_{\text{-}}(t) < \chi_{\text{+}}(t)$ such that $\mathcal{I}(t) = \left]\chi_{\text{-}}(t),\, \chi_{\text{+}}(t)\right[$ and we set $\mathcal{E}(t) := \mathcal{E}^-(t) \cup \mathcal{E}^+(t)$. We consider a conforming partition $\mathscr{T}_h(t) := \left\{\omega_i(t)\right\}_{1 \le i \le n_{\mathrm{el}}}$ of Ω_t into $|\mathscr{T}_h(t)|$ disjoint segments, such that we have $\overline{\Omega_t} = \bigcup_{\omega(t) \in \mathscr{T}_h(t)} \overline{\omega(t)}$.

We make the following additional assumptions:

♯1 $|\mathscr{T}_h(t)| = n_{\mathrm{el}}$ does not vary over time,

♯2 the limit cases $\chi_{\text{-}}(t) \to x_{\mathrm{left}}$ or $\chi_{\text{+}}(t) \to x_{\mathrm{right}}$ do not occur,

♯3 $\mathscr{T}_h(t)$ is compatible with $\mathcal{P}_\Omega(t)$ in the following sense: each mesh element $\omega(t) \in \mathscr{T}_h(t)$ is a subset of only one set of the partition $\mathcal{P}_\Omega(t)$,

the first assumption being not essential for our purpose and could easily be removed. As a consequence, we can write:

$$\mathscr{T}_h(t) = \mathscr{T}_h^e(t) \cup \mathscr{T}_h^i(t), \quad \text{with} \quad \overline{\mathcal{E}(t)} = \bigcup_{\omega(t)\in\mathscr{T}_h^e(t)} \overline{\omega(t)} \quad \text{and} \quad \overline{\mathcal{I}(t)} = \bigcup_{\omega(t)\in\mathscr{T}_h^i(t)} \overline{\omega(t)},$$

where $\mathscr{T}_h^e(t)$ and $\mathscr{T}_h^i(t)$ are respective partitions of the sub-domains $\mathcal{E}(t)$ and $\mathcal{I}(t)$, and at any time $t \in [0, T_{\max}]$, the contact points $\mathcal{K}_-(t), \mathcal{K}_+(t)$ are uniquely identified with some mesh interfaces. For any specified mesh element $\omega_i(t) \in \mathscr{T}_h(t)$, we note $\omega_i(t) = \left]x_{i-\frac{1}{2}}(t),\, x_{i+\frac{1}{2}}(t)\right[$ (with the convention that $x_{\frac{1}{2}} = x_{\text{left}}$, $x_{n_{\text{el}}+\frac{1}{2}} = x_{\text{right}}$), $x_i(t)$ refers to its barycenter, and for any regular enough function $v(\cdot, t)$ defined on $\omega_i(t)$, we define the following jump:

$$\left[\!\left[v(\cdot,t)\right]\!\right]_{\partial\omega_i(t)} := v(\cdot,t)_{|x_{i+\frac{1}{2}}(t)} - v(\cdot,t)_{|x_{i-\frac{1}{2}}(t)}.$$

DG: approximation spaces, basis functions and projectors
For any integer $k \geq 0$, we consider the broken polynomials space defined on the exterior domain:

$$\mathbb{P}^k(\mathscr{T}_h^e(t)) := \left\{ v(\cdot,t) \in L^2(\mathcal{E}(t)),\ \ v_{|\omega(t)} \in \mathbb{P}^k(\omega(t)),\ \ \forall\, \omega(t) \in \mathscr{T}_h^e(t) \right\},$$

where $\mathbb{P}^k(\omega(t))$ denotes the space of polynomials of total degree at most k defined onto $\omega(t)$, with $\dim\left(\mathbb{P}^k(\omega(t))\right) = k+1$. Piecewise polynomial functions belonging to $\mathbb{P}^k(\mathscr{T}_h^e(t))$ are denoted with a subscript h in the following, and for any $\omega(t) \in \mathscr{T}_h^e(t)$ and $v_h(\cdot,t) \in \mathbb{P}^k(\mathscr{T}_h^e(t))$, we may use the convenient shortcut: $v_\omega := v_{h|\omega}$ when no confusion is possible.

For any mesh element $\omega(t) \in \mathscr{T}_h^e(t)$ and any integer $k \geq 0$, we consider a basis for $\mathbb{P}^k(\omega(t))$ denoted by

$$\Psi_\omega(t) := \left\{\psi_j^\omega(\cdot,t)\right\}_{j\in[\![1,\,k+1]\!]}.$$

We observe that we have:

$$\forall t \in [0, T_{\max}], \quad \forall \omega(t) \in \mathscr{T}_h^e(t), \quad \forall j \in [\![1, k+1]\!], \quad \text{supp}(\psi_j^\omega(\cdot,t)) \subset \overline{\omega(t)}.$$

A basis for the global space $\mathbb{P}^k(\mathscr{T}_h^e(t))$ is obtained by gathering the local basis functions:

$$\Psi_h(t) := \bigtimes_{\omega(t)\in\mathscr{T}_h^e(t)} \Psi_\omega(t) = \left\{ \left\{\psi_j^\omega(\cdot,t)\right\}_{j\in[\![1,\,k+1]\!]} \right\}_{\omega(t)\in\mathscr{T}_h(t)}.$$

Remark 2. In what follows, the chosen basis functions are the set of monomials in the physical space. These are defined as follows:

$$\forall \omega_i(t) \in \mathscr{T}_h^e(t),\ \forall j \in [\![1, \ldots, k+1]\!],\ \forall x \in \omega_i(t), \quad \psi_j^{\omega_i}(x,t) := \left(\frac{x - x_i(t)}{|\omega_i(t)|}\right)^j. \tag{15}$$

For any given time value, the degrees of freedom are chosen to be the functionals that map a given discrete unknown belonging to $\mathbb{P}^k(\mathscr{T}_h^e(t))$ to the coefficients of its expansion on the chosen basis functions. Specifically, the degrees of freedom applied to a given function $v_h \in \mathbb{P}^k(\mathscr{T}_h^e)$ return the real numbers

$$\left\{\underline{v}_j^\omega\right\}_{\substack{j\in[\![1,k+1]\!]\\ \omega\in\mathscr{T}_h^e}}, \quad \text{such that} \quad v_\omega := \sum_{j=1}^{k+1} \underline{v}_j^\omega \psi_j^\omega, \quad \forall \omega(t) \in \mathscr{T}_h^e(t). \tag{16}$$

With a little abuse, we refer hereafter to the real numbers (16) as the *degrees of freedom* associated with v_h and we note $\underline{v}_\omega \in \mathbb{R}^{k+1}$ the vector gathering the degrees of freedom associated with v_ω.

For $\omega(t) \in \mathscr{T}_h^e(t)$, we denote by p_ω^k the L^2-orthogonal projector onto $\mathbb{P}^k(\omega(t))$ and $\mathrm{p}_{\mathscr{T}_h^e}^k$ the L^2-orthogonal projector onto $\mathbb{P}^k(\mathscr{T}_h^e(t))$. Similarly, we denote i_ω^k the element nodal interpolator into $\mathbb{P}^k(\omega(t))$, where the nodal distributions in mesh elements are chosen to be the approximate optimal nodes of [3]. The global $\mathrm{i}_{\mathscr{T}_h^e}^k$ interpolator into $\mathbb{P}^k(\mathscr{T}_h^e(t))$ is obtained by gathering the local interpolating polynomials defined on each elements. We also introduce the following shortcut notations for smooth scalar-valued functions:

$$\big(v,w\big)_{\mathscr{T}_h^e(t)} := \sum_{\omega(t)\in\mathscr{T}_h^e(t)} \int_{\omega(t)} v(x,t)w(x,t)\mathrm{d}x, \quad \big\langle \mu,\nu\big\rangle_{\partial\mathscr{T}_h^e(t)} := \sum_{\omega(t)\in\mathscr{T}_h^e(t)} [\![\mu\nu]\!]_{\partial\omega(t)},$$

for $v,w \in L^2(\mathscr{T}_h^e)$ and $\mu,\nu \in L^2(\partial\mathscr{T}_h^e)$. Extensions to vector-valued functions are straightforward. Whenever needed, similar spaces and projectors may be introduced on $\mathcal{I}(t)$.

FV on sub-cells: sub-partitions, sub-resolution basis and sub-mean values
For any mesh element $\omega_i(t) \in \mathscr{T}_h^e(t)$, we introduce a sub-partition $\mathscr{T}_{\omega_i(t)}$ into $k+1$ open disjoint sub-cells:

$$\overline{\omega_i(t)} = \bigcup_{m=1}^{k+1} \overline{S}_m^{\omega_i}(t), \tag{17}$$

where the sub-cell $S_m^{\omega_i}(t) := \left[\widetilde{x}^{\,\omega_i}_{m-\frac{1}{2}}(t), \widetilde{x}^{\,\omega_i}_{m+\frac{1}{2}}(t)\right]$ is of size $\left|S_m^{\omega_i}\right|_\omega = \left|\widetilde{x}^{\,\omega_i}_{m+\frac{1}{2}} - \widetilde{x}^{\,\omega_i}_{m-\frac{1}{2}}\right|$, with the convention $\widetilde{x}^{\,\omega_i}_{\frac{1}{2}} = x_{i-\frac{1}{2}}$ and $\widetilde{x}^{\,\omega_i}_{k+\frac{3}{2}} = x_{i+\frac{1}{2}}$, see Fig. 4. When considering a sequence of neighboring mesh elements $\omega_{i-1}, \omega_i, \omega_{i+1}$, the convenient conventions $S_0^{\omega_i} := S_{k+1}^{\omega_{i-1}}$ and $S_{k+2}^{\omega_i} := S_1^{\omega_{i+1}}$ may be used. For any regular enough function $v(\cdot,t)$ defined on $S_m^\omega(t)$, we use the following shortcut for the sub-cell jump:

$$[\![v(\cdot,t)]\!]_{\partial S_m^\omega(t)} := v(\cdot,t)_{|\widetilde{x}^{\,\omega}_{m+\frac{1}{2}}(t)} - v(\cdot,t)_{|\widetilde{x}^{\,\omega}_{m-\frac{1}{2}}(t)}.$$

For $\omega(t) \in \mathscr{T}_h^e(t)$, we define the *sub-cell indicator* functions $\left\{\mathbb{1}_m^\omega(\cdot,t),\ m \in [\![1,\,k+1]\!]\right\}$ as follows:

$$\mathbb{1}_m^\omega(x,t) := \begin{cases} 1 & \text{if } x \in S_m^\omega(t) \\ 0 & \text{if } x \notin S_m^\omega(t) \end{cases}, \quad \forall m \in [\![1,\,k+1]\!],$$

and the *sub-resolution* basis functions $\left\{\phi_m^\omega(\cdot,t) \in \mathbb{P}^k(\omega(t)),\ m \in [\![1,\,k+1]\!]\right\}$ as follows:

$$\phi_m^\omega(\cdot,t) := p_\omega^k\left(\mathbb{1}_m^\omega(\cdot,t)\right), \quad \forall m \in [\![1,\,k+1]\!]. \tag{18}$$

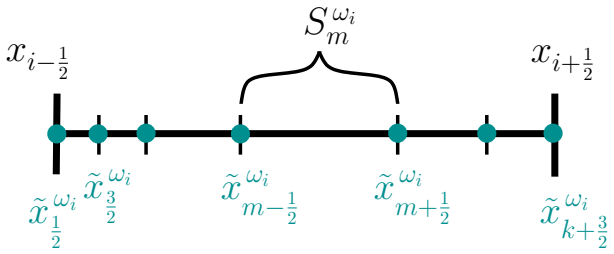

Figure 4: Partition of a mesh element ω_i in $k+1$ sub-cells

One can then check that this definition also entails that for any given value of t:

$$\int_{\omega(t)} \phi_m^\omega \psi \mathrm{d}x = \int_{S_m^\omega(t)} \psi \mathrm{d}x, \quad \forall \psi \in \mathbb{P}^k\left(\omega(t)\right). \tag{19}$$

For any $\omega(t) \in \mathscr{T}_h^e(t)$, we introduce the set of piecewise constant functions on the sub-grid:

$$\mathbb{P}^0(\mathscr{T}_\omega(t)) := \left\{ v(\cdot,t) \in L^2(\omega(t)),\ \ v_{|S_m^\omega} \in \mathbb{P}^0(S_m^\omega(t)),\ \ \forall\, S_m^\omega(t) \in \mathscr{T}_\omega(t) \right\}.$$

For $\omega(t) \in \mathscr{T}_h^e(t)$, and $v_\omega \in \mathbb{P}^k(\omega(t))$, let denote

$$\overline{v}_m^\omega \quad \text{with} \quad m \in [\![1,\, k+1]\!], \tag{20}$$

the lowest-order piecewise constant components defined as the mean-values of v_ω on the sub-cells belonging to the subdivision $\mathscr{T}_\omega(t)$, called *sub-mean values* in the following, which may be gathered in a vector $\overline{v}_\omega \in \mathbb{R}^{k+1}$. Whenever a sequence of neighboring mesh elements $\omega_{i-1}, \omega_i, \omega_{i+1}$ and associated neighboring approximations is considered, the following convenient convention may be used: $\overline{v}_0^{\omega_i} := \overline{v}_{k+1}^{\omega_{i-1}}$ and $\overline{v}_{k+2}^{\omega_i} := \overline{v}_1^{\omega_{i+1}}$.

Remark 3. We observe that any polynomial function $v_\omega \in \mathbb{P}^k(\omega)$ can be expressed equivalently either in terms of the degrees of freedom $\underline{v}^\omega$, or the sub-means values $\overline{v}_\omega$. Indeed, the degrees of freedom $\left\{\underline{v}_m^\omega\right\}_{m\in[\![1,k+1]\!]}$ are uniquely defined through the sub-mean values $\left\{\overline{v}_m^\omega\right\}_{m\in[\![1,k+1]\!]}$, and reversely. Considering the local transformation matrix $\Pi_\omega = \left(\pi_{m,p}^\omega\right)_{m,p}$ defined as:

$$\pi_{m,p}^\omega = \frac{1}{|S_m^\omega(t)|} \int_{S_m^\omega(t)} \psi_p^\omega \mathrm{d}x, \qquad \forall\, (m,p) \in [\![1,\, k+1]\!]^2, \tag{21}$$

the following identities hold:

$$\mathbf{\Pi}_\omega\, \underline{v}_\omega = \overline{v}_\omega \quad \text{and} \quad \mathbf{\Pi}_\omega^{-1}\, \overline{v}_\omega = \underline{v}_\omega.$$

We introduce the (one-to-one) following projector onto the piecewise constant sub-grid space:

$$\begin{aligned} \pi_{\mathscr{T}_\omega}^k : \mathbb{P}^k(\omega(t)) &\to \mathbb{P}^0(\mathscr{T}_\omega(t)) \\ v_h^\omega &\mapsto \pi_{\mathscr{T}_\omega}^k(v_h^\omega) := \overline{v}_\omega. \end{aligned} \tag{22}$$

Time discretization

Concerning time discretization, for a given final computational time $T_{\max} > 0$, we consider a partition $(t^n)_{0\leq n\leq N}$ of the time interval $[0, T_{\max}]$ with $t^0 := 0$, $t^N := T_{\max}$ and $t^{n+1} - t^n =: \Delta t^n$. Details on the computation of the time step Δt^n, related to the choice of the time marching algorithms and some stability requirements, are given in § 3.7. For any sufficiently regular function of time w, we set $w^n := w(t^n)$ and in what follows, such shortcuts relying on a superscript n may be used with any time varying entity, which is evaluated at discrete time t^n. For instance, we set:

$$\mathcal{E}^n := \mathcal{E}(t^n),\ \mathcal{I}^n := \mathcal{I}(t^n),\ \varkappa_-^n := \varkappa_-(t^n),\ \varkappa_+^n := \varkappa_+(t^n),\ \mathscr{T}_h^n := \mathscr{T}_h(t^n),\ \mathscr{T}_h^{e,n} := \mathscr{T}_h^e(t^n),$$

and so on.

3.2. ALE description

In this section, we introduce an ALE description of the coupled problem (11). A central aspect of any ALE description is the construction of a continuous and regular coordinate transformation, allowing to recast the equations from the initial (stationary) domain Ω_0 to the current (moving) domain Ω_t:

$$\Omega_0 \times [0, T_{\max}] \ni (X, t) \ \mapsto\ x(X, t) \in \Omega_t, \tag{23}$$

where X refers to the *reference* coordinate (in the reference frame) and $x := x(X, t)$ the associated *physical* coordinate (in the current frame). Further assuming this mapping to be continuously differentiable with respect to time, piecewise continuously differentiable with respect to X, and denoting by $v_{\mathrm{g}}(x, t)$ the grid's velocity at the physical point $x := x(X, t)$, the following identity holds:

$$v_{\mathrm{g}}(x(X, t), t) = \partial_t x(X, t). \tag{24}$$

Now, for the sake of notations, considering any function $v(x, t)$, let introduce $\widetilde{v}(X, t)$ its counterpart defined on the referential frame as

$$v\left(x(X, t), t\right) =: \widetilde{v}(X, t). \tag{25}$$

Then, for any arbitrary and regular enough function $v(x, t)$, the fundamental ALE relation between the total time derivative, the Eulerian time derivative and the spatial derivative is

$$\frac{\mathrm{d}}{\mathrm{dt}} v\Big(x(X, t), t\Big) := \Big(\partial_t + v_{\mathrm{g}}\, \partial_x\Big) v(x(X, t), t) =: \partial_t \widetilde{v}(X, t). \tag{26}$$

Frame's motion

In order to build such a mapping, for any given time value, the velocity of the contact points may be deduced from the current flow configuration, deriving the free-surface continuity condition (11d) with respect to time, as follows:

$$\Big(\partial_t + v_{\mathrm{g}}\partial_x\Big)\eta^e = \Big(\partial_t + v_{\mathrm{g}}\partial_x\Big)\eta^i \quad \text{on} \quad \varkappa_\pm,$$

so that using the identity $\partial_t \eta^e = -\partial_x q^e$, together with $\partial_t \eta^i = 0$, one has:

$$v_{\mathrm{g}|\varkappa_\pm} = \left(\frac{\partial_x q^e}{\partial_x \eta^e - \partial_x \eta^i}\right)\Big|_{\varkappa_\pm}. \tag{27}$$

Having such contact points velocity at hand, let consider the following smooth diffeomorphism $\chi(\cdot,t):\mathcal{E}_0\to\mathcal{E}(t)$, defined as:

$$\chi(X,t):=\begin{cases} X+\varphi\left(\frac{X-X_0^-}{\varepsilon}\right)\left(\varkappa_-(t)-X_0^-\right) & \text{for} \quad X\in\mathcal{E}_0^-,\\ X+\varphi\left(\frac{X-X_0^+}{\varepsilon}\right)\left(\varkappa_+(t)-X_0^+\right) & \text{for} \quad X\in\mathcal{E}_0^+, \end{cases} \tag{28}$$

where $\varphi\in\mathcal{C}_0^\infty(\mathbb{R})$ is a cut-off function satisfying $\varphi(x)=1$ for $|x|\leq 1$ and $\varepsilon:=\varepsilon_0\ell$ (the reader is referred to Appendix A for the practical definition of φ, ε_0 and Remark 5 for additional considerations regarding the value of ℓ). Then, for any moving grid's interface $x_{i+\frac{1}{2}}(t):=x\big(X_{i+\frac{1}{2}},t\big)$, we define the corresponding interface's velocity as follows:

$$v_{\mathrm{g}_{|i+\frac{1}{2}}}(t):=\widetilde{v_{\mathrm{g}}}(X_{i+\frac{1}{2}},t),$$

with:

$$\widetilde{v_{\mathrm{g}}}(X_{i+\frac{1}{2}},t):=\begin{cases} \partial_t\chi(\cdot,t)_{|X_{i+\frac{1}{2}}}=\begin{cases} \varphi\left(\frac{X_{i+\frac{1}{2}}-X_0^-}{\varepsilon}\right)v_{\mathrm{g}|\varkappa_-} & \text{if} \quad X_{i+\frac{1}{2}}\in\mathcal{E}_0^-,\\ \varphi\left(\frac{X_{i+\frac{1}{2}}-X_0^+}{\varepsilon}\right)v_{\mathrm{g}|\varkappa_+} & \text{if} \quad X_{i+\frac{1}{2}}\in\mathcal{E}_0^+, \end{cases}\\ \dfrac{(X_0^+-X_{i+\frac{1}{2}})}{|\mathcal{I}_0|}v_{\mathrm{g}|\varkappa_-}+\dfrac{(X_{i+\frac{1}{2}}-X_0^-)}{|\mathcal{I}_0|}v_{\mathrm{g}|\varkappa_+} \quad \text{if} \quad X_{i+\frac{1}{2}}\in\mathcal{I}_0. \end{cases} \tag{29}$$

Once the grid's velocity is prescribed at the grid's interfaces, the updated locations of such interfaces may be obtained as the solutions of the following family of IVPs:

$$\begin{cases} \partial_t x(X_{i+\frac{1}{2}},t)=v_{\mathrm{g}_{|i+\frac{1}{2}}}(t),\\ x(X_{i+\frac{1}{2}},0) \quad =X_{i+\frac{1}{2}}. \end{cases} \tag{30}$$

Gathering (27), (29) and solving (30), for any time value, one have available the following sets of discrete grid's interfaces velocities $\left(v_{\mathrm{g}_{|i+\frac{1}{2}}}(t)\right)_{0\leq i\leq n_{\mathrm{el}}}$ and locations $\left(x_{i+\frac{1}{2}}(t)\right)_{0\leq i\leq n_{\mathrm{el}}}$.

Remark 4. The relation (27) is initially well-defined, thanks to the assumption (14) on the initial data. For $t>0$, and under the assumptions recalled in §2.4, the solution of (11)-(13) may exist as long as $\partial_x(\eta^e-\eta^i)_{|\varkappa_\pm}\neq 0$.

Remark 5. Knowing $\varkappa_\pm(t)$, (28) offers a way to dispatch the mesh elements in the moving exterior sub-domain $\mathcal{E}(t)$, avoiding elements collapsing, distorting and related stability issues. We also emphasize that (28) allows to properly deal with the possible occurrence of dry-areas, provided that such areas are initially far enough from the object to prevent the water height from vanishing at contact points. Indeed, assuming that the distance between $\varkappa_\pm(t)$ and the nearest mesh interface where the water height vanishes is greater than ℓ, then (28) ensures that this mesh interface location does not vary over time.

Mapping and geometric parameters

We are now able to provide a suitable definition for the mapping (23) and we consider a piecewise linear and globally continuous transformation such that:

$$x_{|\omega_i(0)}(X,t) := \frac{\left(X_{i+\frac{1}{2}} - X\right)}{|\omega_i(0)|} x_{i-\frac{1}{2}}(t) + \frac{\left(X - X_{i-\frac{1}{2}}\right)}{|\omega_i(0)|} x_{i+\frac{1}{2}}(t), \tag{31}$$

for any $\omega_i(0) := \left[X_{i-\frac{1}{2}}, X_{i+\frac{1}{2}}\right] \in \mathscr{T}_h(0)$. Deriving this definition with respect to time gives:

$$\widetilde{v}_{\mathrm{g}|\omega_i(0)}(X,t) = \frac{(X_{i+\frac{1}{2}} - X)}{|\omega_i(0)|} v_{\mathrm{g}_{|i-\frac{1}{2}}}(t) + \frac{(X - X_{i-\frac{1}{2}})}{|\omega_i(0)|} v_{\mathrm{g}_{|i+\frac{1}{2}}}(t). \tag{32}$$

The deformation gradient associated with the grid's motion is obtained as the Jacobian of this mapping. In particular, we observe that:

$$\partial_X x(X,t)_{|\omega_i(t)} =: \mathcal{J}_{\omega_i(t)} = \frac{|\omega_i(t)|}{|\omega_i(0)|}, \tag{33a}$$

$$\partial_X^k x(X,t)_{|\omega_i(t)} = 0, \ \forall k \geq 2, \tag{33b}$$

so that the mapping is invertible and orientation-preserving. Also, for any $(X_a, X_b) \in (\omega_i(0))^2$, we have:

$$x(X_b,t) = x(X_a,t) + (X_b - X_a)\mathcal{J}_{\omega_i(t)}, \tag{34}$$

and in particular, we deduce that:

$$v_{\mathrm{g}|\omega_i(t)}\big(x,t\big) = \frac{\left(x_{i+\frac{1}{2}}(t) - x\right)}{|\omega_i(t)|} v_{\mathrm{g}_{|i-\frac{1}{2}}}(t) + \frac{\left(x - x_{i-\frac{1}{2}}(t)\right)}{|\omega_i(t)|} v_{\mathrm{g}_{|i+\frac{1}{2}}}(t). \tag{35}$$

Let us recall that the deformation gradient $\mathcal{J}$ satisfies the fundamental relation, generally referred to as Geometric Conservation Law (GCL):

$$\partial_t \, \mathcal{J}(X,t) = \mathcal{J} \, \partial_x v_{\mathrm{g}}(x(X,t),t). \tag{36}$$

Remark 6. It is important to note that the chosen basis functions follow the trajectories. Indeed:

$$\psi_p^{\omega_i}(x,t) = \psi_p^{\omega_i}(x(X,t),t) = \left(\frac{\mathcal{J}(X - X_i)}{\mathcal{J}|\omega_i(0)|}\right)^p = \left(\frac{X - X_i}{|\omega_i(0)|}\right)^p = \widetilde{\psi}_p^{\omega_i}(X),$$

and thus the following fundamental relation is ensured:

$$\forall \omega_i(t) \in \mathscr{T}_h^e(t), \ \forall p \in [\![1, \ldots, k+1]\!], \qquad \frac{\mathrm{d}}{\mathrm{dt}} \, \psi_p^{\omega_i}(x(X,t),t) = 0. \tag{37}$$

This relation also holds for the sub-resolution basis functions ϕ_m^{ω}, *i.e.*:

$$\forall \omega_i(t) \in \mathscr{T}_h^e(t), \ \forall m \in [\![1, \ldots, k+1]\!], \qquad \frac{\mathrm{d}}{\mathrm{dt}} \, \phi_m^{\omega_i}(x(X,t),t) = 0. \tag{38}$$

This property derives from the piecewise linearity of the mapping. Indeed, in this configuration the sub-resolution basis functions can be alternatively defined through their referential frame counterpart as $\phi_m^{\omega}(x(X,t),t) = \widetilde{\phi}_m^{\omega(0)}(X)$, where

$$\widetilde{\phi}_m^{\omega(0)} := \mathrm{p}^k_{\omega(0)}(\mathbb{1}_m^{\omega(0)}), \quad \forall m \in [\![1,\, k+1]\!], \tag{39}$$

which directly implies (38).

Remark 7. Multiplying (11b) by any $\psi(.,t) \in \mathbb{P}^k(\mathscr{T}_h^e(t))$ satisfying $\dfrac{\mathrm{d}}{\mathrm{dt}}\psi(x(X,t),t) = 0$, and integrating over $\omega_i(t)$ gives:

$$\int_{\omega_i(t)} \psi\ \partial_t \mathbf{v}^{\mathrm{e}}\ \mathrm{d}x + \int_{\omega_i(t)} \psi\ \partial_x \mathbf{F}(\mathbf{v}^{\mathrm{e}}, b)\ \mathrm{d}x = \int_{\omega_i(t)} \psi\ \mathbf{B}(\mathbf{v}^{\mathrm{e}}, b')\ \mathrm{d}x. \tag{40}$$

We observe that (36) and (37) lead to the following identity:

$$\frac{\mathrm{d}}{\mathrm{dt}} \int_{\omega_i(t)} \mathbf{v}^{\mathrm{e}}\ \psi\ \mathrm{d}x = \int_{\omega_i(t)} \psi\ \partial_t \mathbf{v}^{\mathrm{e}}\ \mathrm{d}x + \int_{\omega_i(t)} \psi\ \partial_x(\mathbf{v}^{\mathrm{e}} v_{\mathrm{g}})\ \mathrm{d}x,$$

and (40) becomes:

$$\frac{\mathrm{d}}{\mathrm{dt}} \int_{\omega_i(t)} \mathbf{v}^{\mathrm{e}}\ \psi\ \mathrm{d}x + \int_{\omega_i(t)} \psi\ \partial_x \mathbf{G}(\mathbf{v}^{\mathrm{e}}, b, v_{\mathrm{g}})\ \mathrm{d}x = \int_{\omega_i(t)} \psi\ \mathbf{B}(\mathbf{v}^{\mathrm{e}}, b')\ \mathrm{d}x, \tag{41}$$

where we have set $\mathbf{G}(\mathbf{v}^{\mathrm{e}}, b, v_{\mathrm{g}}) := \mathbf{F}(\mathbf{v}^{\mathrm{e}}, b) - \mathbf{v}^{\mathrm{e}} v_{\mathrm{g}}$. Another integration by parts gives:

$$\frac{\mathrm{d}}{\mathrm{dt}} \int_{\omega_i} \mathbf{v}^{\mathrm{e}}\ \psi\ \mathrm{d}x - \int_{\omega_i} \mathbf{G}(\mathbf{v}^{\mathrm{e}}, b, v_{\mathrm{g}})\ \partial_x \psi\ \ \mathrm{d}x + \big[\!\big[\psi\ \mathbf{G}(\mathbf{v}^{\mathrm{e}}, b, v_{\mathrm{g}})\big]\!\big]_{\partial\omega_i(t)} = \int_{\omega_i} \psi\ \mathbf{B}(\mathbf{v}^{\mathrm{e}}, b')\ \mathrm{d}x. \tag{42}$$

3.3. DG-ALE formulation for the fluid/stationary structure model

In this section, we introduce a general DG formulation in ALE description for the fluid-structure problem. Let consider the coupled problem (11), together with initial data as specified in (13) and with the assumptions of §2.4. Then, the associated DG-ALE semi-discrete formulation reads:

$\forall t \in [0, T_{\max}]$, find $\mathbf{v}_h^{\mathrm{e}}(\cdot,t) \in \big(\mathbb{P}^k(\mathscr{T}_h^e(t))\big)^2$, $\mathbf{v}_h^{\mathrm{i}}(\cdot,t) \in \mathbb{P}^k(\mathscr{T}_h^i(t)) \times \mathbb{P}^0(\mathscr{T}_h^i(t))$ and $(\chi_{\text{-}}(t), \chi_{\text{+}}(t)) \in \big]x_{\mathrm{left}}(t),\, x_{\mathrm{right}}(t)\big[^2$ such that, $\forall \varphi_h(\cdot,t) \in \mathbb{P}^k(\mathscr{T}_h^e(t))$ satisfying $\dfrac{\mathrm{d}}{\mathrm{dt}}\varphi_h(x(X,t),t) = 0$, the following system is satisfied:

$$
\begin{cases}
\dfrac{\mathrm{d}}{\mathrm{dt}}\big(\mathbf{v}_h^{\mathrm{e}},\ \varphi_h\big)_{\mathscr{T}_h^e(t)} + \big(\mathcal{A}_h(\mathbf{v}_h^{\mathrm{e}}), \varphi_h\big)_{\mathscr{T}_h^e(t)} = 0, \\
\mathbf{v}_h^{\mathrm{e}}(\cdot,0) \ := \mathrm{p}^k_{\mathscr{T}_h^{e,0}}(\mathbf{v}_0^{\mathrm{e}}), \\
\eta^e_{h|\varkappa_\pm} \quad\ = \eta^i_{h|\varkappa_\pm}, \\
q^e_h(\varkappa_\pm,\cdot) = \underline{q}^i,
\end{cases} \tag{43a}
$$

$$
\begin{cases}
\eta^i_h(\cdot,t) \ := \mathrm{p}^k_{\mathscr{T}_h^i(t)}(\eta^i(\cdot,t)), \\
\dfrac{\mathrm{d}}{\mathrm{dt}}\underline{q}^i(t) = -\Big(\displaystyle\int_{\mathcal{I}(t)} \frac{\mathrm{d}x}{H_h^i}\Big)^{-1} \Big[\!\Big[\frac{1}{2}\Big(\frac{\underline{q}^i(t)}{H_h^i}\Big)^2 + \mathrm{g}\,\eta_h^i\Big]\!\Big]_{\mathcal{I}(t)}, \\
\underline{q}^i(0) \quad := q_0^i,
\end{cases} \tag{43b}
$$

$$
\begin{cases}
\dfrac{\mathrm{d}}{\mathrm{dt}}\varkappa_\pm(t) = v_{\mathrm{g}}(\varkappa_\pm, t), \\
\varkappa_\pm(0) \quad := X_0^\pm,
\end{cases} \tag{43c}
$$

$$
v_{\mathrm{g}|\varkappa_\pm} := \frac{\partial_x q^e_{h|\varkappa_\pm}}{\partial_x \eta^e_{h|\varkappa_\pm} - \partial_x \eta^i_{h|\varkappa_\pm}}, \tag{43d}
$$

$$
b_h(\cdot,t) := \mathrm{I}^k_{\mathscr{T}_h(t)}(b), \tag{43e}
$$

where:

(i) the discrete nonlinear operator $\mathcal{A}_h$ in (43a) is defined by

$$
\big(\mathcal{A}_h(\mathbf{v}_h^{\mathrm{e}}), \varphi_h\big)_{\mathscr{T}_h^e(t)} := -\ \big(\mathbf{G}(\mathbf{v}_h^{\mathrm{e}}, b_h, v_{\mathrm{g}}), \partial_x^h \varphi_h\big)_{\mathscr{T}_h^e(t)} + \big\langle \mathbf{G}^\star, \varphi_h\big\rangle_{\partial\mathscr{T}_h^e(t)} - \big(\mathbf{B}(\mathbf{v}_h^{\mathrm{e}}, b_h'), \varphi_h\big)_{\mathscr{T}_h^e(t)}, \tag{44}
$$

where $\mathbf{G}^\star$ is an interface numerical flux which aims at approximating $\mathbf{F}(\mathbf{v}, b) - v_{\mathrm{g}}\mathbf{v}$ at an interior element boundary moving with the velocity v_{g}, and defined as $\mathbf{G}^\star := \mathbf{F}^\star - v_{\mathrm{g}}\mathbf{v}^\star$, with $\mathbf{F}^\star$ and $\mathbf{v}^\star$ are respectively consistent with $\mathbf{F}$ and $\mathbf{v}$, and computed with the Lax-Friedrichs formula:

$$
\mathbf{F}^\star(\mathbf{v}_R, \mathbf{v}_L, b_R, b_L) := \frac{1}{2}\left(\mathbf{F}(\mathbf{v}_R, b_R) - \mathbf{F}(\mathbf{v}_L, b_L) - \sigma(\mathbf{v}_R - \mathbf{v}_L)\right), \tag{45}
$$

$$
\mathbf{v}^\star(\mathbf{v}_R, \mathbf{v}_L, b_R, b_L) := \frac{1}{2}\left(\mathbf{v}_R + \mathbf{v}_L - \frac{1}{\sigma}\left(\mathbf{F}(\mathbf{v}_R, b_R) - \mathbf{F}(\mathbf{v}_L, b_L)\right)\right), \tag{46}
$$

with

$$
\sigma := \max_{\omega\in\mathscr{T}_h^e}\left(|u^e - v_{\mathrm{g}}| + \sqrt{\mathrm{g}H^e}\right)_{|\partial\omega}. \tag{47}
$$

(ii) we introduce the following projection for η_h^i and interpolation for b_h:

$$
\eta_h^i(\cdot,t) := \mathrm{p}^k_{\mathscr{T}_h^i(t)}(\eta^i), \quad b_h(\cdot,t) := \mathrm{I}^k_{\mathscr{T}_h(t)}(b), \quad H_h^i := \eta_h^i - b_h^i,
$$

where the implicit time dependency of b_h, due to L^2-projections onto time-dependent sub-domains, is made explicit for the sake of clarity. Note that the interpolation of the smooth parameterization b into $\mathbb{P}^k(\mathscr{T}_h)$ is not mandatory, but we choose however to introduce the interpolation of b into $\mathbb{P}^k(\mathscr{T}_h)$, as it allows to preserve the continuity of b at the mesh interfaces (provided that the elements boundary is included into the set of interpolation nodes) and to easily compute a polynomial approximation of the first-order derivative of b.

Remark 8. This general DG-ALE formulation still has to be supplemented with some stabilization process to ensure its robustness and handle the topography variations in a well-balanced way. These issues are addressed in the remainder of this section. A global flowchart of the resulting general algorithm, detailing the processing order of these various numerical ingredients, is also provided in §3.10.

Remark 9. The eigenvalues and eigenvectors of the Jacobian matrix for $\mathbf{F}(\mathbf{v},b)-\mathbf{v}v_{\mathrm{g}}$ are trivially obtained from the NSW system written in ALE description:

$$\frac{\partial\left(\mathbf{F}(\mathbf{v},b)-\mathbf{v}v_{\mathrm{g}}\right)}{\partial\mathbf{v}}(\mathbf{v},b)=\begin{pmatrix} v_{\mathrm{g}} & 1 \\ -u^2+\mathrm{g}H & 2u-v_{\mathrm{g}}\end{pmatrix},$$

leading to the eigenvalues that account for the frame velocity:

$$\lambda^{\pm}:=u-v_{\mathrm{g}}\pm\sqrt{\mathrm{g}H}.$$

Remark 10. The boundary conditions for (43a) are not included into (43), but are classically enforced weakly through the numerical fluxes $\mathbf{G}^{\star}$. As far as boundary conditions are concerned on $\partial\Omega_t$, we may enforce any type of boundary conditions usually available for the NSW equations, including inflow and outflow conditions within subcritical or supercritical configurations relying on local Riemann invariants, periodic conditions or solid-wall conditions.

3.4. DG-ALE as a FV-ALE scheme on sub-cells

It is well-established that the discrete formulation (43a) needs some additional stabilization in order to ensure the positivity of H_h^e at the discrete level, and to avoid Gibbs phenomenon in the vicinity of spatial discontinuities, sharp gradients or smooth extrema. In order to design some suitable correction mechanisms, we show that the FV sub-cell reformulation of the DG method for the NSW equations developed in [14], and initially introduced in [33] for general hyperbolic conservation laws, may be extended to the current DG-ALE framework. We follow the lines of [14] while highlighting the differences due to the frame's motion. Let introduce the following projections onto $\mathbb{P}^k\left(\mathscr{T}_h^e(t)\right)^2$:

$$\mathbf{F}_h^e:=p^k_{\mathscr{T}_h^e(t)}\left(\mathbf{F}(\mathbf{v}_h^{\mathrm{e}},b_h)\right)\quad\text{and}\quad\mathbf{B}_h^e:=p^k_{\mathscr{T}_h^e(t)}\left(\mathbf{B}(\mathbf{v}_h^{\mathrm{e}},b_h')\right),\tag{48}$$

together with the respective shortcuts $\mathbf{F}_{\omega_i(t)}=\mathbf{F}^e_{h|\omega_i(t)}$, $\mathbf{B}_{\omega_i(t)}=\mathbf{B}^e_{h|\omega_i(t)}$, $\mathbf{G}_{\omega_i}=\mathbf{F}_{\omega_i}-v_{\mathrm{g}}\mathbf{v}_{\omega_i}$. We substitute these projections into (43a) and integrate by parts the second term to obtain, for all $\psi\in\mathbb{P}^k\left(\mathscr{T}_h^e(t)\right)$ satisfying $\dfrac{\mathrm{d}}{\mathrm{d}t}\psi\left(x(X,t),t\right)=0$:

$$\frac{\mathrm{d}}{\mathrm{d}t}\int_{\omega_i(t)}\mathbf{v}^{\mathrm{e}}_{\omega_i}\psi\,\mathrm{d}x=-\int_{\omega_i(t)}\partial_x\mathbf{G}_{\omega_i}\psi\,\mathrm{d}x+\left[\!\left[(\mathbf{G}_{\omega_i}-\mathbf{G}^{\star})\psi\right]\!\right]_{\partial\omega_i(t)}+\int_{\omega_i(t)}\mathbf{B}_{\omega_i}\psi\,\mathrm{d}x.\tag{49}$$

For a given mesh element $\omega(t)\in\mathscr{T}_h^e(t)$, we consider a sub-partition $\mathscr{T}_\omega(t)$ defined in (17), together with the sub-resolution basis functions (18). Substituting $\psi=\phi_m^{\omega_i}$ into (49), for all m in

$[\![1,\dots,k+1]\!]$, recalling the definition of the sub-mean values $\overline{\mathbf{v}}_m^{\omega_i}$ in (20), recalling also that $\mathbf{v}_{\omega_i}$, $\partial_x(\mathbf{v}_{\omega_i} v_{\mathrm{g}})$, $\partial_x \mathbf{F}_{\omega_i}$ and $\mathbf{B}_{\omega_i}$ all belong to $\mathbb{P}^k\left(\omega_i(t)\right)^2$ and finally using identity (19), the following discrete formulation holds, for all m in $[\![1,\dots,k+1]\!]$:

$$\frac{\mathrm{d}}{\mathrm{dt}}\left(|S_m^{\omega_i}(t)|\overline{\mathbf{v}}_m^{\omega_i}\right) = -\left[\!\left[\mathbf{G}_{\omega_i}\right]\!\right]_{\partial S_m^{\omega}(t)} + \left[\!\left[(\mathbf{G}_{\omega_i}-\mathbf{G}^\star)\phi_m^{\omega_i}\right]\!\right]_{\partial\omega_i(t)} + |S_m^{\omega_i}(t)|\,\overline{\mathbf{B}}_m^{\omega_i}. \tag{50}$$

We introduce the $k+2$ sub-cell's *reconstructed fluxes*, denoted by $\left\{\widehat{\mathbf{G}}_{m+\frac{1}{2}}^{\omega_i}\right\}_{m\in[\![0,\,k+1]\!]}$, and defined as the solution of the following linear system:

$$\widehat{\mathbf{G}}_{m+\frac{1}{2}}^{\omega_i} - \widehat{\mathbf{G}}_{m-\frac{1}{2}}^{\omega_i} := \left[\!\left[\mathbf{G}_{\omega_i}\right]\!\right]_{\partial S_m^{\omega}(t)} - \left[\!\left[(\mathbf{G}_{\omega_i}-\mathbf{G}^\star)\phi_m^{\omega_i}\right]\!\right]_{\partial\omega_i(t)}, \quad \forall m\in[\![1,\,k+1]\!],$$

$$\widehat{\mathbf{G}}_{\frac{1}{2}}^{\omega_i} := \mathbf{G}_{i-\frac{1}{2}}^\star \qquad \text{and} \qquad \widehat{\mathbf{G}}_{k+3/2}^{\omega_i} := \mathbf{G}_{i+\frac{1}{2}}^\star,$$

so that (43a) may be recast as a FV-ALE formulation on the sub-partition:

$$\frac{\mathrm{d}}{\mathrm{dt}}\left(|S_m^{\omega_i}(t)|\overline{\mathbf{v}}_m^{\omega_i}\right) = -\left(\widehat{\mathbf{G}}_{m+\frac{1}{2}}^{\omega_i} - \widehat{\mathbf{G}}_{m-\frac{1}{2}}^{\omega_i}\right) + |S_m^{\omega_i}(t)|\overline{\mathbf{B}}_m^{\omega_i}, \quad \forall m\in[\![1,\,k+1]\!]. \tag{51}$$

Remark 11. For practical purpose, an explicit formula for the computation of the interior reconstructed fluxes for $m\in[\![1,\dots,k]\!]$ is:

$$\widehat{\mathbf{G}}_{m+\frac{1}{2}}^{\omega_i} = \mathbf{G}_{\omega_i}\left(\widetilde{x}_{m+\frac{1}{2}}\right) - c_{m+\frac{1}{2}}^{i-\frac{1}{2}}\left(\mathbf{G}_{\omega_i}\left(x_{i-\frac{1}{2}}\right) - \mathbf{G}_{i-\frac{1}{2}}^\star\right) - c_{m+\frac{1}{2}}^{i+\frac{1}{2}}\left(\mathbf{G}_{\omega_i}\left(x_{i+\frac{1}{2}}\right) - \mathbf{G}_{i+\frac{1}{2}}^\star\right), \tag{52}$$

with

$$c_{m+\frac{1}{2}}^{i-\frac{1}{2}} = \sum_{p=m+1}^{k+1}\phi_p^{\omega_i}\left(x_{i-\frac{1}{2}}\right) \qquad \text{and} \qquad c_{m+\frac{1}{2}}^{i+\frac{1}{2}} = \sum_{p=1}^{m}\phi_p^{\omega_i}\left(x_{i+\frac{1}{2}}\right). \tag{53}$$

Simple explicit expression of the correction coefficients can be found in [33].

Remark 12. We require that the integrals and source term in (43a) are exactly computed at motionless steady states. This can be achieved, thanks to the pre-balanced formulation of the NSW equations, by using any quadrature rule that is exact for polynomials of degree up to $2\,k$. Let us recall that $2\,k$ is in any case the minimum requirement to reach the expected $k+1$ order of accuracy.

3.5. Sub-cell low-order corrected FV-ALE fluxes

In this section, we show that the reconstructed fluxes may be locally corrected to enforce some required properties. As investigated in [14] for the NSW equations, lowest-order FV fluxes may be introduced in order to: (i) prevent high-order approximations from spurious oscillations in the vicinity of discontinuities and sharp gradients, (ii) ensure the preservation of the water height's positivity. Additionally, one needs to introduce some states reconstructions, inspired from [24] in order to ensure a well-balancing property. In what follows, we recall the definition of such corrected fluxes, highlighting the new terms associated with the frame's motion. The specification of suitable admissibility criteria is postponed to the next section.

For any time value $t \in [0, T_{\max}]$, $\omega_i(t) \in \mathscr{T}_h^e(t)$, and any marked sub-cell $S_m^{\omega_i}(t) \in \mathscr{T}_{\omega_i(t)}$, let define the sub-partition interface values for b, where the subscript ω_i and the time dependency are forgotten for the sake of simplicity:

$$\overline{b}_{m+\frac{1}{2}} := \max(\overline{b}_m, \overline{b}_{m+1}), \quad \overline{b}_m^{\pm} := \overline{b}_{m\pm\frac{1}{2}} - \max\left(0, \overline{b}_{m\pm\frac{1}{2}} - \overline{\eta}_m\right).$$

sub-cell's interfaces reconstructions for the water height are defined as follows:

$$\overline{H}_m^{\pm} := \max\left(0, \overline{\eta}_m - \overline{b}_{m\pm\frac{1}{2}}\right),$$

and the corresponding free-surface elevation and discharge are deduced as follows:

$$\overline{\eta}_m^{\pm} := \overline{H}_m^{\pm} + \overline{b}_m^{\pm}, \qquad \overline{q}_m^{\pm} := \overline{H}_m^{\pm} \frac{\overline{q}_m}{\overline{H}_m}, \qquad \overline{\mathbf{v}}_m^{\pm} := (\overline{\eta}_m^{\pm}, \overline{q}_m^{\pm}), \tag{54}$$

where $\overline{b}_m^{\pm}$ refer to the trace of $\overline{b}_m$ at the sub-cell's interfaces. Related lowest-order numerical fluxes on sub-cell's $S_m(t)$ left and right interfaces are built accordingly:

$$\mathcal{F}_{m+\frac{1}{2}}^l := \mathbf{F}^\star\left(\overline{\mathbf{v}}_m^+, \overline{\mathbf{v}}_{m+1}^-, \overline{b}_m^+, \overline{b}_m^+\right) + \begin{pmatrix} 0 \\ \mathrm{g}\overline{\eta}_m^+\left(\overline{b}_m^+ - b_{\widetilde{x}_{m+\frac{1}{2}}}\right) \end{pmatrix}, \tag{55}$$

$$\mathcal{F}_{m-\frac{1}{2}}^r := \mathbf{F}^\star\left(\overline{\mathbf{v}}_{m-1}^+, \overline{\mathbf{v}}_m^-, \overline{b}_m^-, \overline{b}_m^-\right) + \begin{pmatrix} 0 \\ \mathrm{g}\overline{\eta}_m^-\left(\overline{b}_m^- - b_{\widetilde{x}_{m-\frac{1}{2}}}\right) \end{pmatrix}, \tag{56}$$

where $b_{\widetilde{x}_{m\pm\frac{1}{2}}}$ are respectively the interpolated polynomial values of b_h at $\widetilde{x}_{m+\frac{1}{2}}$ and $\widetilde{x}_{m-\frac{1}{2}}$. The associated numerical flux, in the ALE description, are deduced as follows:

$$\mathcal{G}_{m+\frac{1}{2}}^l := \mathcal{F}_{m+\frac{1}{2}}^l - v_{\mathrm{g}_{|m+\frac{1}{2}}} \mathbf{v}_{m+\frac{1}{2}}^{\star,l}, \quad \text{and} \quad \mathcal{G}_{m-\frac{1}{2}}^r := \mathcal{F}_{m-\frac{1}{2}}^r - v_{\mathrm{g}_{|m-\frac{1}{2}}} \mathbf{v}_{m-\frac{1}{2}}^{\star,r}, \tag{57}$$

with

$$\mathbf{v}_{m+\frac{1}{2}}^{\star,l} := \mathbf{v}^\star\left(\overline{\mathbf{v}}_m^+, \overline{\mathbf{v}}_{m+1}^-, \overline{b}_m^+, \overline{b}_m^+\right), \quad \text{and} \quad \mathbf{v}_{m-\frac{1}{2}}^{\star,r} := \mathbf{v}^\star\left(\overline{\mathbf{v}}_{m-1}^+, \overline{\mathbf{v}}_m^-, \overline{b}_m^-, \overline{b}_m^-\right). \tag{58}$$

Using such corrected FV-ALE fluxes, it is possible to modify the reconstructed fluxes $\widehat{\mathbf{G}}_{m+\frac{1}{2}}$ in a robust way, in some particular sub-cells, where the *uncorrected* DG scheme (51) has failed to produce an admissible solution. We are thus left with the issues of identifying the local sub-cells that may need some corrections and defining a robust correction procedure, which are respectively addressed in §3.6 and §3.8.

3.6. Admissibility criteria

A large number of sensors or detectors have been introduced in the literature in order to identify the particular cells/sub-cells in which some additional stabilization mechanisms are required. We use two admissibility criteria: one for the *Physical Admissibility Detection* (PAD) and the other to address the occurrence of spurious oscillations, called *sub-cell Numerical Admissibility Detection* (SubNAD). This last criterion is supplemented with a relaxation procedure to exclude the smooth extrema from the troubled cells. These criteria, which definitions are not recalled in the present work, are detailed in [14].

3.7. Time marching algorithm

So far, we only consider a semi-discrete spatial discretization. When fully-discrete formulations are considered, the time-stepping may be carried out using explicit Strong-Stability-Preserving Runge-Kutta (SSP-RK) schemes, [11, 28], and following the notations introduced in §3.1, we denote the time-dependency on discrete time t^n with a superscript n:

$$\mathbf{v}_h^{\mathrm{e},n} := \mathbf{v}_h^{\mathrm{e}}(\cdot, t^n), \quad \underline{q}^{i,n} := \underline{q}^i(t^n), \quad \varkappa_{\pm}^n := \varkappa_{\pm}(t^n).$$

Writing the semi-discrete equation (43a) in the operator form

$$\partial_t \mathbf{v}_h^{\mathrm{e}} + \mathcal{A}_h(\mathbf{v}_h^{\mathrm{e}}) = 0,$$

we advance the discrete solution $\mathbf{v}_h^{\mathrm{e},n} \in \left(\mathbb{P}^k\left(\mathscr{T}_h^{e,n}\right)\right)^2$ from time level n to level $(n+1)$, with $\mathbf{v}_h^{\mathrm{e},n+1} \in \left(\mathbb{P}^k(\mathscr{T}_h^{e,n+1})\right)^2$, through the a SSP-RK scheme. Let us explicit the third-order RK case:

$$\begin{aligned}
\mathbf{v}_h^{e,n,(1)} &= \mathbf{v}_h^{e,n} - \Delta t^n \mathcal{A}_h(\mathbf{v}_h^{e,n}),\\
\mathbf{v}_h^{e,n,(2)} &= \frac{1}{4}(3\mathbf{v}_h^{e,n} + \mathbf{v}_h^{e,n,(1)}) - \frac{1}{4}\Delta t^n \mathcal{A}_h(\mathbf{v}_h^{e,n,(1)}),\\
\mathbf{v}_h^{e,n+1} &= \frac{1}{3}(\mathbf{v}_h^{e,n} + 2\mathbf{v}_h^{e,n,(2)}) - \frac{2}{3}\Delta t^n \mathcal{A}_h(\mathbf{v}_h^{e,n,(2)}),
\end{aligned}$$

where $\mathbf{v}_h^{e,n,(i)}$, $1 \le i \le 2$, are the solutions obtained at intermediate stages, Δt^n is obtained from the CFL condition (59). As the stability enforcement operator described in the previous sections relies on both DG approximations on mesh elements $\omega^n \in \mathscr{T}_h^{e,n}(t)$ and FV scheme on the sub-cells $S_m^{\omega,n} \in \mathscr{T}_\omega^n$, the time step Δt^n is computed adaptively using the following CFL condition:

$$\Delta t^n = \frac{\min\limits_{\omega^n \in \mathscr{T}_h^{e,n}} \left(\dfrac{h_\omega^n}{2k+1}, \min\limits_{S_m^{\omega,n} \in \mathscr{T}_\omega^n} |S_m^{\omega,n}| \right)}{\sigma}, \tag{59}$$

where σ is the constant previously introduced in (47). The same SSP-RK method for the discretization of equations of type (30) leads to the following discrete algorithm:

$$\begin{aligned}
x^{n,(1)} &= x^n + \Delta t^n v_{\mathrm{g}}^n,\\
x^{n,(2)} &= \frac{3x^n + x^{n,(1)}}{4} + \frac{\Delta t^n}{4} v_{\mathrm{g}}^{n,(1)},\\
x^{n+1} &= \frac{x^n + 2x^{n,(2)}}{3} + \frac{2\Delta t^n}{3} v_{\mathrm{g}}^{n,(2)}.
\end{aligned} \tag{60}$$

Reversely, one may compute the grid's interfaces velocity from their locations as follows:

$$\begin{aligned}
v_{\mathrm{g}}^n &= \frac{x^{n,(1)} - x^n}{\Delta t^n},\\
v_{\mathrm{g}}^{n,(1)} &= \frac{4x^{n,(2)} - 3x^n - x^{n,(1)}}{\Delta t^n},\\
v_{\mathrm{g}}^{n,(2)} &= \frac{3x^{n+1} - x^n - 2x^{n,(2)}}{2\Delta t^n}.
\end{aligned} \tag{61}$$

3.8. A posteriori Local Sub-cell Correction (LSC) method

Gathering all the previous ingredients, we introduce a global algorithm that ensures the stability and robustness of the flow's computation in $\mathcal{E}(t)$. This algorithm is adapted from [14] and extended to the current DG-ALE framework. We only provide a qualitative description and focus on the steps that require further comments, due to the additional ALE description. Starting from an admissible piecewise polynomial approximate solution $\mathbf{v}_h^{e,n} \in \left(\mathbb{P}^k(\mathscr{T}_h^{e,n})\right)^2$ at discrete time t^n, we first compute a *predictor candidate solution* $\mathbf{v}_h^{e,n+1} \in \left(\mathbb{P}^k(\mathscr{T}_h^{n+1})\right)^2$ at time t^{n+1} using the uncorrected DG-ALE scheme (44), together with the corresponding SSP-RK time discretization of §3.7. Then, for any mesh element $\omega_i^{n+1} \in \mathscr{T}_h^{e,n+1}$, we compute the predictor candidate sub-mean values:

$$\mathbb{P}^0(\mathscr{T}_{\omega_i}^{e,n+1}) \ni \overline{\mathbf{v}}_{\omega_i}^{e,n+1} = \pi_{\mathscr{T}_{\omega_i}^{e,n+1}}(\mathbf{v}_{\omega_i}^{e,n+1}).$$

For any sub-cell $S_m^{\omega_i,n+1} \in \mathscr{T}_{\omega_i}^{n+1}$, we check admissibility of the associated sub-mean values $\overline{\mathbf{v}}_m^{\omega_i,n+1}$ using the criteria of §3.6. For a given sub-cell $S_m^{\omega_i,n+1}$ that needs additional stabilization, the corresponding DG *reconstructed interface fluxes* $\widehat{\mathbf{G}}_{m\pm\frac{1}{2}}$ defined in (52), which were initially used to compute the predictor candidate $\mathbf{v}_h^{e,n+1}$, will be replaced by the FV *corrected fluxes* $\mathcal{G}_{m\pm\frac{1}{2}}^{l/r}$ of (57) into the update process to compute a new candidate sub-cell value through the local FV-ALE formulation (51). As we want the *a posteriori* LSC method to ensure conservation at the sub-cell level, the left and right sub-cells of a troubled one have to be also recomputed through a FV-like scheme but this time with possibly only one high-order reconstructed flux to be replaced by a first-order one. Let us emphasize that for the remaining sub-cells, nothing has to be done and their associated mean value will be the one obtained through the uncorrected DG scheme. For more details on the *a posteriori* LSC method , we refer to [33, 14]. The complete set of substituting rules is not recalled here, but concisely, the new updating process for sub-cell value $\overline{\mathbf{v}}_m^{\omega_i,n+1}$ may fall into one of the following alternative:

$$i)\quad \frac{\mathrm{d}}{\mathrm{dt}}\left(|S_m^{\omega_i}(t)|\overline{\mathbf{v}}_m^{\omega_i}\right) = -\left(\mathcal{G}_{m+\frac{1}{2}}^{l} - \mathcal{G}_{m-\frac{1}{2}}^{r}\right) + |S_m^{\omega_i}(t)|\overline{\mathbf{B}}_m^{\omega_i}, \tag{62a}$$

$$ii)\quad \frac{\mathrm{d}}{\mathrm{dt}}\left(|S_m^{\omega_i}(t)|\overline{\mathbf{v}}_m^{\omega_i}\right) = -\left(\mathcal{G}_{m+\frac{1}{2}}^{l} - \widehat{\mathbf{G}}_{m-\frac{1}{2}}^{\omega_i}\right) + |S_m^{\omega_i}(t)|\overline{\mathbf{B}}_m^{\omega_i}, \tag{62b}$$

$$iii)\quad \frac{\mathrm{d}}{\mathrm{dt}}\left(|S_m^{\omega_i}(t)|\overline{\mathbf{v}}_m^{\omega_i}\right) = -\left(\widehat{\mathbf{G}}_{m+\frac{1}{2}}^{\omega_i} - \mathcal{G}_{m-\frac{1}{2}}^{r}\right) + |S_m^{\omega_i}(t)|\overline{\mathbf{B}}_m^{\omega_i}. \tag{62c}$$

For mesh elements $\omega_i(t)$ in which such fluxes corrections have occurred, leading to the computation of updated/limited sub-mean values, a new high-order polynomial candidate solution, still denoted by $\mathbf{v}_h^{e,n+1}$ for the sake of simplicity, is built upon these updated sub-mean values:

$$\mathbb{P}^k(\omega_i^n) \ni \mathbf{v}_{\omega_i}^{e,n+1} = \pi^{-1}_{\mathscr{T}_{\omega_i}^{n+1}}(\overline{\mathbf{v}}_{\omega_i}^{e,n+1}),$$

and the process may go further in time after checking that this new candidate is admissible.

The whole detection-correction-projection iterative process may be conveniently summarized through the application of a stabilization/correction operator denoted as follows:

$$\begin{aligned} \Lambda_h^{k,n} \;:\; \left(\mathbb{P}^k\left(\mathscr{T}_h^{e,n}\right)\right)^2 &\;\to\; \left(\mathbb{P}^k\left(\mathscr{T}_h^{e,n}\right)\right)^2, \\ \mathbf{v}_h^{e,n} &\;\mapsto\; \Lambda_h^{k,n}(\mathbf{v}_h^{e,n}), \end{aligned} \tag{63}$$

where the resulting broken polynomial $\Lambda_h^{k,n}(\mathbf{v}_h^{e,n})$ satisfies all the admissibility criteria, see §3.6. Embedding such a stabilization operator into a fully discrete version of (43a), with for instance a third order SSP-RK method, would simply gives:

$$\begin{aligned}
\mathbf{v}_h^{e,n,(1)} &= \Lambda_h^{k,n,(1)}\Big(\mathbf{v}_h^{e,n} - \Delta t^n \mathcal{A}_h(\mathbf{v}_h^{e,n})\Big),\\
\mathbf{v}_h^{e,n,(2)} &= \Lambda_h^{k,n,(2)}\Big(\frac{1}{4}(3\mathbf{v}_h^{e,n} + \mathbf{v}_h^{e,n,(1)}) - \frac{1}{4}\Delta t^n \mathcal{A}_h(\mathbf{v}_h^{e,n,(1)})\Big),\\
\mathbf{v}_h^{e,n+1} &= \Lambda_h^{k,n+1}\Big(\frac{1}{3}(\mathbf{v}_h^{e,n} + 2\mathbf{v}_h^{e,n,(2)}) - \frac{2}{3}\Delta t^n \mathcal{A}_h(\mathbf{v}_h^{e,n,(2)})\Big).
\end{aligned} \tag{64}$$

3.9. Properties of the DG-ALE formulation with a posteriori LSC

In this section, we show that the resulting global fully discrete DG-ALE scheme with *a posteriori* LSC is globally well-balanced for motionless steady states and satisfies the DGCL.

Well-balancing for motionless steady states

Let begin with the well-balanced property. Motionless steady states for problem (11) are trivially defined as follows:

$$\mathbf{v}^{\mathrm{e}}(\cdot,t) = \mathbf{v}^{\mathrm{c}} = \begin{pmatrix}\eta^{\mathrm{c}}\\ 0\end{pmatrix}, \quad \underline{q^i}(t) = 0, \quad \chi_{\pm}(t) = X_0^{\pm}, \quad \forall t \geq 0. \tag{65}$$

We highlight that proving that the global semi-discrete formulation (43) preserves such steady states is equivalent to prove that the DG-ALE scheme (43a) is well-balanced on $\mathcal{E}(t) = \mathcal{E}^-(t) \cup \mathcal{E}^+(t)$, which again reduces to ensure the property on $\mathcal{E}^-(t)$ and $\mathcal{E}^+(t)$ separately. Indeed, it is straightforward to observe that at steady states, (43b)-(43c) lead to

$$\frac{\mathrm{d}}{\mathrm{d}t}\underline{q^i}(t) = 0, \qquad v_{\mathrm{g}|\chi_{\pm}}(t) = 0, \qquad \eta^i_{\chi_{\pm}} = \eta^{\mathrm{c}},$$

so that the coupling with the partially immersed object actually does not disturb the flow steady state, thanks to the discontinuous nature of the approximation. Hence, we have the following result for the first-order in time fully discrete formulation:

Proposition 13. The discrete formulation (43) with possible occurrence of local corrected lowest-order fluxes in one of the three possible formulations (62a)-(62b)-(62c), together with a first-order Euler time-marching algorithm, preserves the motionless steady states (65), provided that the integrals of (43a) are exactly computed at motionless steady states. Specifically, for all $n \geq 0$,

$$\left(\eta_h^{\mathrm{e},n} = \eta^c \text{ and } q_h^{\mathrm{e},n} = 0\right) \implies \left(\eta_h^{\mathrm{e},n+1} = \eta^c \text{ and } q_h^{\mathrm{e},n+1} = 0\right).$$

Proof. At steady states, for any given t and any mesh element $\omega(t)$, we have

$$\partial_x \mathbf{F}(\mathbf{v}_{\omega(t)}, b_{\omega(t)}) = \mathbf{B}(\mathbf{v}_{\omega(t)}, b'_{\omega(t)}). \tag{66}$$

Furthermore, both $\mathbf{F}(\mathbf{v}_h^{\mathrm{e}}, b_h)$ and $\mathbf{B}(\mathbf{v}_h^{\mathrm{e}}, b'_h)$ belong to $\left(\mathbb{P}^k(\mathscr{T}_h^e(t))\right)^2$ so that we have:

$$\mathbf{F}_h := p^k_{\mathscr{T}_h^e(t)}(\mathbf{F}(\mathbf{v}_h^{\mathrm{e}}, b_h)) = \mathbf{F}(\mathbf{v}_h^{\mathrm{e}}, b_h), \tag{67}$$

$$\mathbf{B}_h := p^k_{\mathscr{T}_h^e(t)}(\mathbf{B}(\mathbf{v}_h^{\mathrm{e}}, b'_h)) = \mathbf{B}(\mathbf{v}_h^{\mathrm{e}}, b'_h). \tag{68}$$

We also emphasize that it is equivalent to prove the property for the formulation (51) on the sub-partitions or for the formulation (43a) on $\mathscr{T}_h^{e,n}$. We choose to work with (51) to show that the scheme is well-balanced even at the sub-cell level, and we drop the superscript e in the remainder of this proof for the sake of simplicity:

$$\begin{aligned} &\forall \omega^n \in \mathscr{T}_h^{e,n}, \quad \forall m \in [\![1,\dots,k+1]\!], \;\; \overline{\eta}_m^{\omega,n} = \eta^c, \;\; \overline{q}_m^{\omega,n} = 0 \\ &\qquad \Longrightarrow \quad \forall \omega^{n+1} \in \mathscr{T}_h^{e,n+1}, \quad \forall m \in [\![1,\dots,k+1]\!], \;\; \overline{\eta}_m^{\omega,n+1} = \eta^c, \quad \overline{q}_m^{\omega,n+1} = 0. \end{aligned} \tag{69}$$

As stated in §3.8, investigating the various possibilities for the definition of the interface fluxes implies to investigate the "uncorrected" situation (51) (corresponding to high-order DG reconstructed fluxes at all sub-cells interfaces) plus three "corrected" situations enumerated in (62a)-(62b)-(62c) (and corresponding to the occurrence of modified lowest-order FV fluxes at (some of) the sub-cells interfaces). As (62b) and (62c) boil down to the same situation with a permutation of left and right fluxes, we have, for any given value $m \in [\![1,\dots,k+1]\!]$, to distinguish three different situations:

case 1 - admissible sub-cell: $S_{m-1}^{\omega_i}$, $S_m^{\omega_i}$ and $S_{m+1}^{\omega_i}$ are all admissible. The sub-cell mean value $\overline{\mathbf{v}}_m^{\omega_i,n+1}$ is then one obtained through the uncorrected DG scheme. Equivalently, the local time-update formula with reconstructed fluxes writes

$$|S_m^{\omega_i,n+1}|\,\overline{\mathbf{v}}_m^{\omega_i,n+1} = |S_m^{\omega_i,n}|\,\overline{\mathbf{v}}_m^{\omega_i,n} - \Delta t^n\big(\widehat{\mathbf{G}}_{m+\frac{1}{2}}^{\omega_i} - \widehat{\mathbf{G}}_{m-\frac{1}{2}}^{\omega_i}\big) + \Delta t^n |S_m^{\omega_i,n}|\,\overline{\mathbf{B}}_m^{\omega_i}. \tag{70}$$

where $\widehat{\mathbf{G}}_{m+\frac{1}{2}}^{\omega_i}$ and $\widehat{\mathbf{G}}_{m-\frac{1}{2}}^{\omega_i}$ are defined in (52). We observe that at steady state:

$$\eta_{i\pm\frac{1}{2}}^{+} = \eta_{i\pm\frac{1}{2}}^{-} = \eta^c, \qquad q_{i\pm\frac{1}{2}}^{+} = q_{i\pm\frac{1}{2}}^{-} = 0, \qquad \text{and} \qquad b_{i\pm\frac{1}{2}}^{+} = b_{i\pm\frac{1}{2}}^{-},$$

and therefore,

$$\mathbf{F}_{i\pm\frac{1}{2}}^{\star} = \begin{pmatrix} 0 \\ \frac{1}{2}\mathrm{g}\eta^c\big(\eta^c - 2b_{i\pm\frac{1}{2}}\big) \end{pmatrix} = \mathbf{F}\big(\mathbf{v}_{\omega_i|x_{i\pm\frac{1}{2}}}, b_{\omega_i|x_{i\pm\frac{1}{2}}}\big), \tag{71}$$

and,

$$\mathbf{v}_{i\pm\frac{1}{2}}^{\star} = \begin{pmatrix} \eta^c \\ 0 \end{pmatrix} = \mathbf{v}_{\omega_i|x_{i\pm\frac{1}{2}}},$$

resulting in

$$\mathbf{G}_{i\pm\frac{1}{2}}^{\star} = \mathbf{F}\Big(\mathbf{v}_{\omega_i|x_{i\pm\frac{1}{2}}}, b_{\omega_i|x_{i\pm\frac{1}{2}}}\Big) - v_{g_{|i\pm\frac{1}{2}}}\mathbf{v}_{\omega_i|x_{i\pm\frac{1}{2}}}. \tag{72}$$

Using (67), we also have:

$$\mathbf{G}_{\omega_i|x_{i\pm\frac{1}{2}}} = \mathbf{F}\Big(\mathbf{v}_{\omega_i|x_{i\pm\frac{1}{2}}}, b_{\omega_i|x_{i\pm\frac{1}{2}}}\Big) - v_{g_{|i\pm\frac{1}{2}}}\mathbf{v}_{\omega_i|x_{i\pm\frac{1}{2}}}, \tag{73}$$

thus, using the definition (52) of $\widehat{\mathbf{G}}_{m\pm\frac{1}{2}}^{\omega_i}$, we obtain:

$$\widehat{\mathbf{G}}_{m\pm\frac{1}{2}}^{\omega_i} = \mathbf{G}_{\omega_i|\widetilde{x}_{m\pm\frac{1}{2}}} = \mathbf{F}\Big(\mathbf{v}_{\omega_i|\widetilde{x}_{m\pm\frac{1}{2}}}, b_{\omega_i|\widetilde{x}_{m\pm\frac{1}{2}}}\Big) - v_{g_{|i\pm\frac{1}{2}}}\mathbf{v}_{\omega_i|\widetilde{x}_{m\pm\frac{1}{2}}}, \tag{74}$$

allowing to compute the difference:

$$\widehat{\mathbf{G}}^{\omega_i}_{m+\frac{1}{2}} - \widehat{\mathbf{G}}^{\omega_i}_{m-\frac{1}{2}} = \int_{S^i_m} \partial_x \mathbf{F}(\mathbf{v}_{\omega_i}, b_{\omega_i})\, \mathrm{d}x - (v_{\mathrm{g}_{|m+\frac{1}{2}}} - v_{\mathrm{g}_{|m-\frac{1}{2}}})\mathbf{v}^c. \tag{75}$$

Additionally, updating in time the frame's interfaces with a first-order Euler scheme leads to:

$$x^{n+1} = x^n + \Delta t^n v^n_{\mathrm{g}},$$

so that the geometric term may be simplified as follows:

$$(v_{\mathrm{g}_{|m+\frac{1}{2}}} - v_{\mathrm{g}_{|m-\frac{1}{2}}})\, \mathbf{v}^c = \frac{\widetilde{x}^{n+1}_{m+\frac{1}{2}} - \widetilde{x}^{n+1}_{m-\frac{1}{2}} - (\widetilde{x}^{n}_{m+\frac{1}{2}} - \widetilde{x}^{n}_{m-\frac{1}{2}})}{\Delta t^n}\mathbf{v}^c = \frac{|S^{\omega_i,n+1}_m| - |S^{\omega_i,n}_m|}{\Delta t^n}\mathbf{v}^c.$$

Finally, (70) writes:

$$\begin{aligned}|S^{\omega_i,n+1}_m|\, \overline{\mathbf{v}}^{\omega_i,n+1}_m = |S^{\omega_i,n}_m|\, \mathbf{v}^c - \Delta t^n \left(\int_{S^{\omega_i,n}_m} \partial_x \mathbf{F}(\mathbf{v}^n_{\omega_i}, b_{\omega_i}) - \mathbf{B}(\mathbf{v}^n_{\omega_i}, \partial_x b_{\omega_i})\, \mathrm{d}x \right) \\ + |S^{\omega_i,n+1}_m|\, \mathbf{v}^c - |S^{\omega_i,n}_m|\, \mathbf{v}^c,\end{aligned}$$

and using (66), we obtain:

$$\overline{\mathbf{v}}^{\omega_i,n+1}_m = \mathbf{v}^c = \overline{\mathbf{v}}^{\omega_i,n}_m. \tag{76}$$

case 2 - neighbor of a non-admissible sub-cell: $S^{\omega_i}_m$, $S^{\omega_i}_{m-1}$ are admissible but $S^{\omega_i}_{m+1}$ is non-admissible (the symmetric situation of $S^{\omega_i}_m$, $S^{\omega_i}_{m+1}$ are admissible but $S^{\omega_i}_{m-1}$ is non-admissible may be treated in a similar way). The corresponding time-update formula is :

$$|S^{\omega_i,n+1}_m|\, \overline{\mathbf{v}}^{\omega_i,n+1}_m = |S^{\omega_i,n}_m|\, \overline{\mathbf{v}}^{\omega_i,n}_m - \Delta t^n \big(\mathcal{G}^{\omega_i,l}_{m+\frac{1}{2}} - \widehat{\mathbf{G}}^{\omega_i}_{m-\frac{1}{2}}\big) + \Delta t^n |S^{\omega_i,n}_m|\, \overline{\mathbf{B}}^{\omega_i}_m, \tag{77}$$

with $\mathcal{G}^{\omega_i,l}_{m+\frac{1}{2}}$ and $\widehat{\mathbf{G}}^{\omega_i}_{m-\frac{1}{2}}$ defined in (55)-(57) and (52). To evaluate $\mathcal{G}^{\omega_i,l}_{m+\frac{1}{2}}$ at steady state, we observe that $\overline{\eta}^+_m = \overline{\eta}^-_{m+1} = \eta^c$, leading to:

$$\mathbf{F}^\star\left(\overline{\mathbf{v}}^+_m, \overline{\mathbf{v}}^-_{m+1}, \overline{b}^+_m, \overline{b}^+_m\right) = \frac{1}{2}\begin{pmatrix} 0 \\ \mathrm{g}\eta^c\left(\eta^c - 2\overline{b}^+_m\right)\end{pmatrix},$$

and

$$\mathcal{F}^{\omega_i,l}_{m+\frac{1}{2}} = \mathbf{F}\Big(\mathbf{v}_{\omega_i|\widetilde{x}_{m+\frac{1}{2}}}, b_{\omega_i|\widetilde{x}_{m+\frac{1}{2}}}\Big). \tag{78}$$

As we also have

$$\mathbf{v}^{\star,l}_{m+\frac{1}{2}} = \mathbf{v}^\star\left(\overline{\mathbf{v}}^+_m, \overline{\mathbf{v}}^-_{m+1}, \overline{b}^+_m, \overline{b}^+_m\right) = \mathbf{v}_{\omega_i|\widetilde{x}_{m+\frac{1}{2}}},$$

we obtain

$$\mathcal{G}^{\omega_i,l}_{m+\frac{1}{2}} = \mathbf{F}\Big(\mathbf{v}_{\omega_i|\widetilde{x}_{m+\frac{1}{2}}}, b_{\omega_i|\widetilde{x}_{m+\frac{1}{2}}}\Big) - v_{\mathrm{g}_{|m+\frac{1}{2}}}\mathbf{v}_{\omega_i|\widetilde{x}_{m+\frac{1}{2}}}.$$

The computation of $\widehat{\mathbf{G}}^{\omega_i}_{m-\frac{1}{2}}$ is performed as in **case 1**, leading to (74) and we may evaluate the difference as follows:

$$\mathcal{G}^{\omega_i,l}_{m+\frac{1}{2}} - \widehat{\mathbf{G}}^{\omega_i}_{m-\frac{1}{2}} = \int_{S^{\omega_i}_m} \partial_x \mathbf{F}(\mathbf{v}_{\omega_i}, b_{\omega_i})\, \mathrm{d}x - (v_{\mathrm{g}_{|m+\frac{1}{2}}} - v_{\mathrm{g}_{|m-\frac{1}{2}}})\, \mathbf{v}^c, \tag{79}$$

so that,

$$\overline{\mathbf{v}}^{\omega_i,n+1}_m = \mathbf{v}^c = \overline{\mathbf{v}}^{\omega_i,n}_m.$$

case 3 - corrected sub-cell: $S^{\omega_i}_m$ is non-admissible. The time-update formula is:

$$|S^{\omega_i,n+1}_m|\, \overline{\mathbf{v}}^{\omega_i,n+1}_m = |S^{\omega_i,n}_m|\, \overline{\mathbf{v}}^{\omega_i,n}_m - \Delta t^n \big(\mathcal{G}^{\omega_i,l}_{m+\frac{1}{2}} - \mathcal{G}^{\omega_i,r}_{m-\frac{1}{2}}\big) + \Delta t^n |S^{\omega_i,n}_m|\, \overline{\mathbf{B}}^{\omega_i}_m. \tag{80}$$

with $\mathcal{G}^{\omega_i,l}_{m+\frac{1}{2}}$ and $\mathcal{G}^{\omega_i,r}_{m-\frac{1}{2}}$ defined in (57). Reproducing the computation steps as in **case 2**, we obtain:

$$\mathcal{G}^{\omega_i,l}_{m+\frac{1}{2}} = \mathbf{F}\Big(\mathbf{v}_{\omega_i|\widetilde{x}_{m+\frac{1}{2}}}, b_{\omega_i|\widetilde{x}_{m+\frac{1}{2}}}\Big) - v_{\mathrm{g}_{|m+\frac{1}{2}}} \mathbf{v}_{\omega_i|\widetilde{x}_{m+\frac{1}{2}}}, \tag{81}$$

$$\mathcal{G}^{\omega_i,r}_{m-\frac{1}{2}} = \mathbf{F}\Big(\mathbf{v}_{\omega_i|\widetilde{x}_{m-\frac{1}{2}}}, b_{\omega_i|\widetilde{x}_{m-\frac{1}{2}}}\Big) - v_{\mathrm{g}_{|m-\frac{1}{2}}} \mathbf{v}_{\omega_i|\widetilde{x}_{m-\frac{1}{2}}}, \tag{82}$$

and

$$\mathcal{G}^{\omega_i,l}_{m+\frac{1}{2}} - \mathcal{G}^{\omega_i,r}_{m-\frac{1}{2}} = \int_{S^{\omega_i}_m} \partial_x \mathbf{F}(v_{\omega_i}, b_{\omega_i})\, \mathrm{d}x - (v_{\mathrm{g}_{|m+\frac{1}{2}}} - v_{\mathrm{g}_{|m-\frac{1}{2}}})\, \mathbf{v}^c, \tag{83}$$

so that,

$$\overline{\mathbf{v}}^{\omega_i,n+1}_m = \mathbf{v}^c = \overline{\mathbf{v}}^{\omega_i,n}_m.$$

□

Remark 14. This well-balanced property can be extended to any higher-order SSP-RK time discretization as those methods can be expressed as a convex combination of first-order Euler schemes.

Discrete Geometric Conservation Law (DGCL)

In simulations of free-surface flows involving free moving boundaries, it is important to ensure that the proposed numerical scheme in ALE description exactly preserves uniform flows. Such preservation property is called Geometric Conservation Law in the literature and simply states that the moving mesh procedure does not disturb the uniform flow configuration. Hence, considering $\Omega_t = \mathcal{E}(t)$ (no object) and $b = 0$, we inject a constant solution $\mathbf{v}^{\mathrm{e}}_h(\cdot, t) = (\eta^{\mathrm{c}}, q^{\mathrm{c}})$ into (43a), together with

$$\varphi_h(x,t) := \mathbb{1}^{\omega_i}(x,t) = \begin{cases} 1 & \text{if} \quad x \in \omega_i(t) \\ 0 & \text{if} \quad x \notin \omega_i(t) \end{cases},$$

to obtain:

$$\mathbf{v}^c \frac{\mathrm{d}}{\mathrm{dt}} \int_{\omega_i(t)} \mathrm{d}x = -\big[\!\big[\mathbf{F}(\mathbf{v}^c, 0) - v_{\mathrm{g}} \mathbf{v}^c\big]\!\big]_{\partial\omega_i(t)} = \mathbf{v}^c\, \big[\!\big[v_{\mathrm{g}}\big]\!\big]_{\partial\omega_i(t)},$$

and thus the GCL reduces to the following (automatically satisfied) property:

$$\frac{\mathrm{d}\,|\omega_i(t)|}{\mathrm{dt}} = \big[\!\big[v_{\mathrm{g}}\big]\!\big]_{\partial\omega_i(t)}. \tag{84}$$

At the fully discrete level, we show that a fully discrete formulation, relying on an high-order SSP Runge-Kutta time discretization, satisfies the DGCL.

Proposition 15. The DG-ALE semi-discrete scheme (43a), together with SSP-RK time-marching algorithm and the embedded stabilization operator with possible occurrence of corrected lowest-order fluxes in one of the following formulations (62a)-(62b)-(62c), preserves the Discrete Geometric Conservation Law. Specifically, assuming $b = 0$, we have, for any discrete time t^n:

$$\left(\mathbf{v}_h^{\mathrm{e},n} = \mathbf{v}^{\mathrm{c}}\right) \implies \left(\mathbf{v}_h^{\mathrm{e},n+1} = \mathbf{v}^{\mathrm{c}}\right).$$

Proof. Under the assumption $\mathbf{v}_h^{\mathrm{e},n} = \mathbf{v}^{\mathrm{c}}$, we have $\mathbf{F}(\mathbf{v}_h^{\mathrm{e}}, b_h) \in \left(\mathbb{P}^k(\mathscr{T}_h^{e,n})\right)^2$, and we observe that the following identity holds:

$$\mathbf{F}_h^n := p^k_{\mathscr{T}_h^{e,n}}(\mathbf{F}(\mathbf{v}_h^{\mathrm{e},n}, b_h)) = \mathbf{F}(\mathbf{v}_h^{\mathrm{e},n}, b_h). \tag{85}$$

As in the proof of Proposition 13, it is equivalent to show that the property holds at the sub-cell level, using formulation (51). Let us emphasize that Proposition 15 holds for any SSP-RK time discretization. The demonstration will be here specified for the third-order SSP-RK case. Let denote by $|S_m^{\omega_i,(1)}|$, $|S_m^{\omega_i,(2)}|$, and $|S_m^{\omega_i,n+1}|$ the length of the sub-cell $S_m^{\omega_i}$ at the three different time stages (and whenever the RK stage dependency has to be specified, we apply the superscripts $(.)^{(1)}$, $(.)^{(2)}$ and $(.)^{n+1}$ to the concerned quantities). The 3^{rd} order SSP-RK discretization reads as follows:

$$\begin{cases} |S_m^{\omega_i,(1)}|\mathbf{v}_m^{\omega_i,(1)} = |S_m^{\omega_i,n}|\mathbf{v}_m^{\omega_i,n} + \Delta t^n \mathcal{R}_m^{\omega_i,n}, \\ \\ |S_m^{\omega_i,(2)}|\mathbf{v}_m^{\omega_i,(2)} = \dfrac{3|S_m^{\omega_i,n}|\mathbf{v}_m^{\omega_i,n} + |S_m^{\omega_i,(1)}|\mathbf{v}_m^{\omega_i,(1)}}{4} + \dfrac{\Delta t^n}{4}\mathcal{R}_m^{\omega_i,(1)}, \\ \\ |S_m^{\omega_i,n+1}|\mathbf{v}_m^{\omega_i,n+1} = \dfrac{|S_m^{\omega_i,n}|\mathbf{v}_m^{\omega_i,n} + 2|S_m^{\omega_i,(2)}|\mathbf{v}_m^{\omega_i,(2)}}{3} + \dfrac{2\Delta t^n}{3}\mathcal{R}_m^{\omega_i,(2)}. \end{cases} \tag{86}$$

We have, for any given value $m \in [\![1, \ldots, k+1]\!]$, to distinguish three different cases:
case 1 - admissible sub-cell: $S_{m-1}^{\omega_i}$, $S_m^{\omega_i}$ and $S_{m+1}^{\omega_i}$ are all admissible. The residual $\mathcal{R}_m^{\omega_i,(j)}$ is:

$$\mathcal{R}_m^{\omega_i,(j)} = -\left(\widehat{\mathbf{G}}_{m+\frac{1}{2}}^{\omega_i,(j)} - \widehat{\mathbf{G}}_{m-\frac{1}{2}}^{\omega_i,(j)}\right), \tag{87}$$

As we assume $\mathbf{v}_h^{\mathrm{e},n} = \mathbf{v}^c$, using (85), we get :

$$\widehat{\mathbf{G}}_{m\pm\frac{1}{2}}^{\omega_i,n} = \mathbf{G}_{\omega_i|\widetilde{x}_{m\pm\frac{1}{2}}}^n = \mathbf{F}\left(\mathbf{v}^c, 0\right) - v_{\mathrm{g}_{|m\pm\frac{1}{2}}}^n \mathbf{v}^c,$$

so that

$$\widehat{\mathbf{G}}_{m+\frac{1}{2}}^{\omega_i,n} - \widehat{\mathbf{G}}_{m-\frac{1}{2}}^{\omega_i,n} = (v_{\mathrm{g}_{|m+\frac{1}{2}}}^n - v_{\mathrm{g}_{|m-\frac{1}{2}}}^n)\mathbf{v}^{\mathrm{c}}.$$

Using the SSP-RK time update of the grid velocity (61), we obtain:

$$\begin{aligned} |S_m^{\omega_i,(1)}|\mathbf{v}_m^{\omega_i,(1)} &= |S_m^{\omega_i,n}|\mathbf{v}^{\mathrm{c}} + \Delta t^n \left(\frac{\widetilde{x}_{m+\frac{1}{2}}^{(1)} - \widetilde{x}_{m+\frac{1}{2}}^n - \widetilde{x}_{m-\frac{1}{2}}^{(1)} + \widetilde{x}_{m-\frac{1}{2}}^n}{\Delta t^n}\right)\mathbf{v}^{\mathrm{c}} \\ &= |S_m^{\omega_i,n}|\mathbf{v}^{\mathrm{c}} + |S_m^{\omega_i,(1)}|\mathbf{v}^{\mathrm{c}} - |S_m^{\omega_i,n}|\mathbf{v}^{\mathrm{c}}, \\ &= |S_m^{\omega_i,(1)}|\mathbf{v}^{\mathrm{c}}, \end{aligned}$$

and therefore:

$$\mathbf{v}_m^{\omega_i,(1)} = \mathbf{v}^c.$$

In a similar way, we show that $\mathbf{v}_m^{\omega_i,(2)} = \mathbf{v}^c$ and $\mathbf{v}_m^{\omega_i,n+1} = \mathbf{v}^c$, leading to the desired conclusion.

case 2 - corrected sub-cell: $S_m^{\omega_i}$ is non-admissible. The residual $\mathcal{R}_m^{\omega_i,(j)}$ is:

$$\mathcal{R}_m^{\omega_i,(j)} = -\left(\mathcal{G}_{m+\frac{1}{2}}^{l,\omega_i,(j)} - \mathcal{G}_{m-\frac{1}{2}}^{r,\omega_i,(j)}\right), \tag{88}$$

and one can show that we have:

$$\mathcal{G}_{m+\frac{1}{2}}^{l,\omega_i,n} = \mathbf{F}\left(\mathbf{v}^c, 0\right) - v_{\mathrm{g}_{|m+\frac{1}{2}}}^n \mathbf{v}^c, \quad \text{and} \quad \mathcal{G}_{m-\frac{1}{2}}^{l,\omega_i,n} = \mathbf{F}\left(\mathbf{v}^c, 0\right) - v_{\mathrm{g}_{|m-\frac{1}{2}}}^n \mathbf{v}^c,$$

leading to

$$\mathcal{G}_{m+\frac{1}{2}}^{l,\omega_i,n} - \mathcal{G}_{m-\frac{1}{2}}^{r,\omega_i,n} = (v_{\mathrm{g}_{|m+\frac{1}{2}}}^n - v_{\mathrm{g}_{|m-\frac{1}{2}}}^n)\mathbf{v}^c,$$

and therefore

$$\mathbf{v}_m^{\omega_i,n+1} = \mathbf{v}^c.$$

case 3 - neighbor of a non-admissible sub-cell: $S_m^{\omega_i}$, $S_{m-1}^{\omega_i}$ are admissible but $S_{m+1}^{\omega_i}$ is non-admissible (the symmetric situation of $S_m^{\omega_i}$, $S_{m+1}^{\omega_i}$ are admissible but $S_{m-1}^{\omega_i}$ is non-admissible may be treated in a similar way). The residual $\mathcal{R}_m^{\omega_i,(j)}$ in a mixed DG/FV context is:

$$\mathcal{R}_m^{\omega_i,(j)} = -\left(\widehat{\mathbf{G}}_{m+\frac{1}{2}}^{\omega_i,(j)} - \mathcal{G}_{m-\frac{1}{2}}^{r,\omega_i,(j)}\right). \tag{89}$$

As in the two previous situations, we have:

$$\widehat{\mathbf{G}}_{m+\frac{1}{2}}^{\omega_i,n} = \mathbf{F}\left(\mathbf{v}^c, 0\right) - v_{\mathrm{g}_{|m+\frac{1}{2}}}^n \mathbf{v}^c,$$
$$\mathcal{G}_{m-\frac{1}{2}}^{r,\omega_i,,n} = \mathbf{F}\left(\mathbf{v}^c, 0\right) - v_{\mathrm{g}_{|m-\frac{1}{2}}}^n \mathbf{v}^c,$$

leading to

$$\widehat{\mathbf{G}}_{m+\frac{1}{2}}^{\omega_i,n} - \mathcal{G}_{m-\frac{1}{2}}^{r,\omega_i,n} = (v_{\mathrm{g}_{|m+\frac{1}{2}}}^n - v_{\mathrm{g}_{|m-\frac{1}{2}}}^n)\mathbf{v}^c,$$

so that,

$$\mathbf{v}_m^{\omega_i,n+1} = \mathbf{v}^c.$$

□

3.10. Flowchart

Let summarize the global numerical strategy associated with (43) for the simulation of free-surface waves and a stationary partly immersed object interactions in shallow water. For the sake of simplicity, a first-order Euler time-marching scheme is assumed to produce some fully discrete approximations. This procedure may be straightforwardly extended to higher-order time-marching algorithms.

Starting from available and admissible values of $\mathbf{v}_h^{\mathrm{e},n}$, $\varkappa_{\pm}^n$, $\underline{q}^{i,n}$, $\eta_h^{i,n} := \mathrm{p}_{\mathscr{T}_h^{i,n}}^k(\eta^i)$, $b_h^n := \mathrm{I}_{\mathscr{T}_h^n}^k(b)$,

1. locally compute the frame's velocity at contact points $v_{\mathrm{g}_{|\varkappa_{\pm}}}^n$ using (27),

2. globally compute the frame's velocity v_{g}^n for all mesh interfaces for $\mathscr{T}_h^{e,n}$ and $\mathscr{T}_h^{i,n}$, using (29),
3. globally compute the updated locations of mesh interfaces at discrete time $t = t^{n+1}$ using the frame's velocity v_{g}^n and the family of IVP (30). In particular, the updated positions of the contact points $\chi_{\pm}^{n+1}$ are obtained,
4. from the set of discrete values for grid points velocity and interfaces location, we reconstruct continuous profiles for both quantities inside mesh elements using (31) and (32), in order to qualify updated quadrature nodes or sub-cells interfaces and compute velocities at these points (used in the definition of numerical fluxes),
5. compute the updated solution $\mathbf{v}_h^{\mathrm{e},n+1}$ and $\underline{q}^{i,n+1}$ while accounting for the geometric terms related to the displacement of the mesh, as well as for the stabilization procedure. Increment time and cycle to step 1.

4. Numerical validations

In this section, we provide several numerical assessments of the DG-ALE discrete formulation (43). In the following test-cases, if not stated differently, we display sub-mean values instead of point-wise values of the polynomial approximations, as it allows to precisely illustrate the sub-cell resolution of the scheme. Also, in the following numerical validations, we choose to consider partially immersed objects with elliptic profiles. Such a choice is of course arbitrary and may be straightforwardly adapted to alternative object's profiles. The reader is referred to the Appendix B for explicit formula.

4.1. Dam-break over a flat bottom

This first test-case is dedicated to the numerical assessment of the DG-ALE implementation with *a posteriori* LSC method for the NSW model and we consider classical dam-break problems over a flat bottom, without incorporating any partially immersed structure for the time being. Hence we only consider the formulation (43a) associated with the shallow water equations, considering that $\mathcal{E}(t) = \Omega$, and replacing the coupling conditions at the free boundaries by classical homogeneous Neumann boundary conditions for the NSW equations. The computational domain is defined as $\Omega = [0, 1]$ and the initial data is defined as follows:

$$\eta_0(x) := \left\{ \begin{array}{ll} 1 & \text{if} \quad x \leq 0.5, \\ 0.5 & \text{elsewhere,} \end{array} \right. , \qquad q_0 := 0, \qquad b := 0.$$

We set $T_{\max} = 0.075\, s$, $n_{\mathrm{el}} = 50$, $k = 3$ and *for this particular test-case only*, the frame's velocity is defined in a *pseudo-Lagrangian* way, directly connected to the fluid's local velocity as follows:

$$v_{\mathrm{g}_{|i+\frac{1}{2}}} := \frac{1}{2}\left(u^+_{i+\frac{1}{2}} + u^-_{i+\frac{1}{2}} - \frac{1}{\sigma}\left(\mathbf{F}^q(\mathbf{v}^+_{i+\frac{1}{2}}, b_{i+\frac{1}{2}}) - \mathbf{F}^q(\mathbf{v}^-_{i+\frac{1}{2}}, b_{i+\frac{1}{2}}) \right) \right), \tag{90}$$

where $u^{\pm}_{i+\frac{1}{2}}$ are the left and right traces of the fluid's velocity at the mesh interface $x_{i+\frac{1}{2}}$ and σ is defined as $\sigma := \max_{\omega \in \mathscr{T}_h} \sigma_\omega$ with

$$\sigma_\omega := \max_m \left(\sqrt{g \overline{H}^{\omega}_m} \right).$$

We show on Fig. 5-left a snapshot of the free-surface at $t = 0.075\, s$ and we highlight the *corrected* and *uncorrected* sub-cells on the right. This illustrates that the correction is activated only in a very thin area in the vicinity of the discontinuity, preventing the occurrence of spurious oscillations.

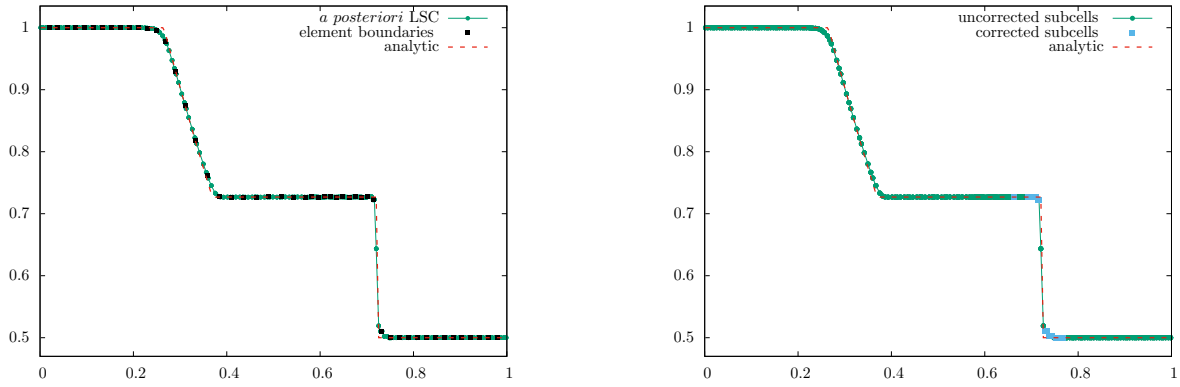

Figure 5: Test 1 - Dam break over a flat bottom - Free-surface elevation computed at $t = 0.075\,s$, for $k = 3$ and $n_{\text{el}} = 50$ (left). The corrected and uncorrected sub-cells are displayed on the right.

4.2. Well-balancing property

In this second test-case, we aim at assessing the motionless steady-states preservation property. This property has already been studied for the DG method with *a posteriori* LSC method in [14] and, as a consequence, we only consider the validation of the following new features: (i) the case of a moving grid without incorporated object, (ii) the case of a partially immersed object over a varying bottom. Firstly, we consider the computational domain $\Omega = [0, 1]$ without any immersed object, together with a varying bottom defined as follows:

$$b(x) := \begin{cases} A\left(\sin\left(\dfrac{(x - x_1)\cdot\pi}{75}\right)\right)^2 & \text{if} \quad x_1 \leq x \leq x_2, \\ 0 & \text{elsewhere,} \end{cases} \tag{91}$$

where $A = 4.75$, $x_1 = 0.125\,m$ and $x_2 = 0.875\,m$, and the initial data is defined as:

$$\eta_0 := 10, \qquad q_0 := 0,$$

see Fig. 6. We set $k = 3$, $n_{\text{el}} = 50$ and *for this particular test-case only*, the grid's velocity is uniformly defined as $v_{\text{g}} := 0.01\ \text{m}\cdot\text{s}^{-1}$. We evolve in time the initial data up to 10^6 time iterations, which correspond to $T_{\max} = 50\,s$, and we observe that this initial data is preserved up to machine precision. We also observe that the initial computational domain Ω_0 is translated of $0.5\,m$ after $50\,s$ of time evolution. A similar behavior is of course reported for alternate combinations of k, n_{el} and v_{g}.

In a second configuration, we introduce a partially immersed object, together with a dry-area. The computational domain is $\Omega := [-50, 200]$ and the object is located at $(x_G, z_G) := (50, H_0 + 2.5)$. The topography profile is defined as follows:

$$b(x) := \begin{cases} A\left(\sin\left(\dfrac{(x - x_1)\cdot\pi}{75}\right)\right)^2 & \text{if} \quad x_1 \leq x \leq x_2, \\ \dfrac{1}{\beta}\,(x - x_3) & \text{if} \quad x \geq x_3, \\ 0 & \text{elsewhere,} \end{cases} \tag{92}$$

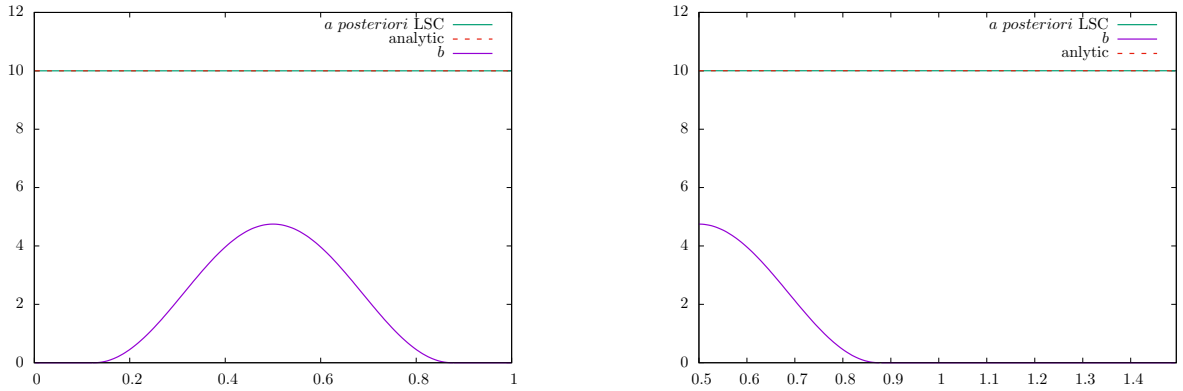

Figure 6: Test 2 - Preservation of a motionless steady state with a moving frame - Free-surface elevation at $t_0 = 0\,s$ (left), and $T_{\max} = 50\,s$ (right).

where $A = 1.5\,m$, $\beta = 11$, $x_1 = 12.5\,m$, $x_2 = 87.5\,m$ and $x_3 = 90\,m$. Initial data in $\mathcal{E}_0$ are defined as

$$\eta_0^e(x) := \max\left(5.0, b(x)\right) \qquad \text{and} \qquad q_0^e := 0,$$

while in the interior domain $\mathcal{I}_0$ we set:

$$\eta_0^i := \mathrm{p}^k_{\mathscr{T}_h^{\mathrm{i},0}}(\eta_{\mathrm{lid}}) \qquad \text{and} \qquad q_0^i := 0.$$

We evolve this initial configuration up to $T_{\max} = 50\,s$, with $k = 3$, $n_{\mathrm{el}}^e = 50$ and $n_{\mathrm{el}}^i = 10$. The free-surface elevation obtained with the DG-ALE scheme using the *a posteriori* LSC method is shown on Fig. 7. The corrected and uncorrected sub-cells are exhibited on Fig. 8, with a zoom in the vicinity of the object. The motionless steady state is preserved up to the machine accuracy and this feature can be reproduced with any other choices for k, n_{el}^e and n_{el}^i.

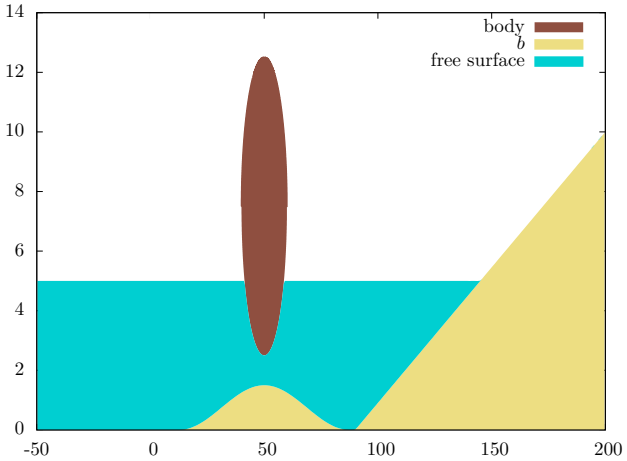

Figure 7: Test 2 - Preservation of a motionless steady state with a stationary object - Free-surface elevation at $T_{\max} = 50\,s$, with $k = 3$, $n_{\mathrm{el}}^e = 50$, $n_{\mathrm{el}}^i = 10$.

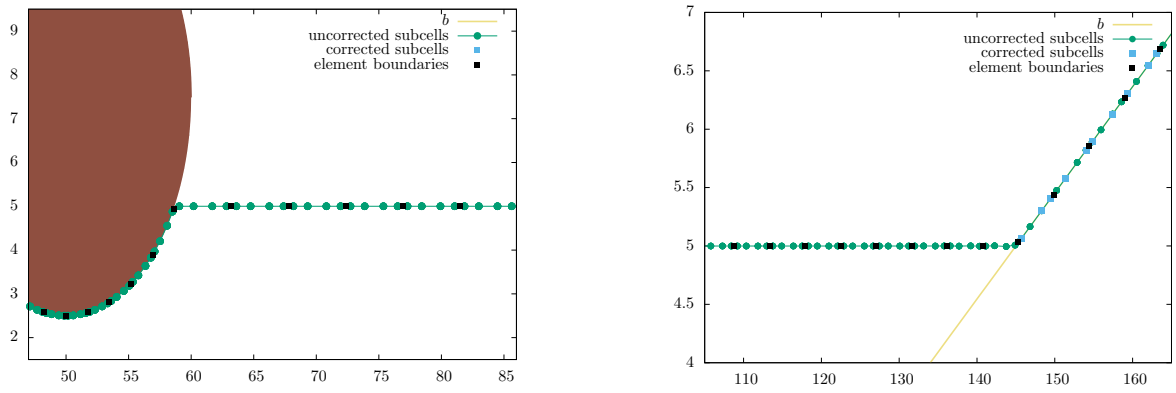

Figure 8: Test 2 - Preservation of a motionless steady state with a stationary object - Free-surface elevation at $T_{\max} = 50\,s$, with a zoom near the object (left) and the shoreline (right), showing the corrected and the uncorrected sub-cells, for $k = 3$, $n^e_{\text{el}} = 50$, $n^i_{\text{el}} = 10$.

4.3. A solitary wave interacting with a stationary object

In this third test-case, we focus on the interactions between a weakly nonlinear solitary wave propagating towards a stationary partially immersed object, over a varying topography made of a bump followed by a sloping beach. We consider the computational domain $\Omega := [0, 100]$, with $H_0 = 5\,m$ and the topography profile is defined as follows:

$$b(x) := \begin{cases} A_b \left(\sin\left(\dfrac{(x - x_1) \cdot \pi}{75} \right) \right)^2 & \text{if} \quad x_1 \leq x \leq x_2, \\ 0 & \text{elsewhere,} \end{cases} \tag{93}$$

where $A_b = 1.5\,m$, $x_1 = 12.5\,m$ and $x_2 = 87.5\,m$. A stationary object is placed over the bump and the initial data is prescribed as follows:

$$\eta^e_0(x) := H_0 + A_w \operatorname{sech}\left(\gamma\,(x - x_0)\right), \qquad q^e_0(x) := \mathrm{g} c_{q_2} (\eta^e_0(x) - H_0) H^e_0,$$

and

$$\eta^i_0 := \mathrm{p}^k_{\mathscr{T}^{\mathrm{i},0}_h}(\eta_{\mathrm{lid}}), \qquad q^i_0 := 0,$$

where $A_w = 0.35\,m$, $c_{q_1} = 1$, $c_{q_2} = 0.5$, $\gamma := c_{q_1}\sqrt{\dfrac{3A_w}{4H_0}}$ and $x_0 = 20\,m$ stands for the initial location of the solitary wave's center. The elliptic object is defined with respective horizontal and vertical radius $a = 10\,m$ and $b = 5\,m$, and its center of mass is located at $(x_{\mathrm{G}}, z_{\mathrm{G}}) = (50, H_0 + 2.5)$ (see Appendix B for the explicit definition of the object and the parameterization of its underside). We set $n^e_{\text{el}} = 50$, $n^i_{\text{el}} = 10$ and $k = 3$. Snapshots of the free-surface at various times during the propagation are shown on Fig. 9, together with the corresponding values of the discharge, and the normalized pressure beneath the object. Interestingly, we observe a partial run-up, run-down and reflection on the object's left side. This reflected wave goes back towards the inlet boundary, while the transmitted wave propagates further beyond the object, into the right exterior domain, finally, both reflected and transmitted wave are evacuated from the computational domain, thanks to the Neumann boundary conditions on $\partial\Omega_t$. In order to exhibit some quantitative informations regarding the accuracy of the resulting approximation, we gather in Table 1 the global L^2-errors computed for an increasing number of elements and $k = 3$, for the inner pressure at $T_{\max} = 100\,s$.

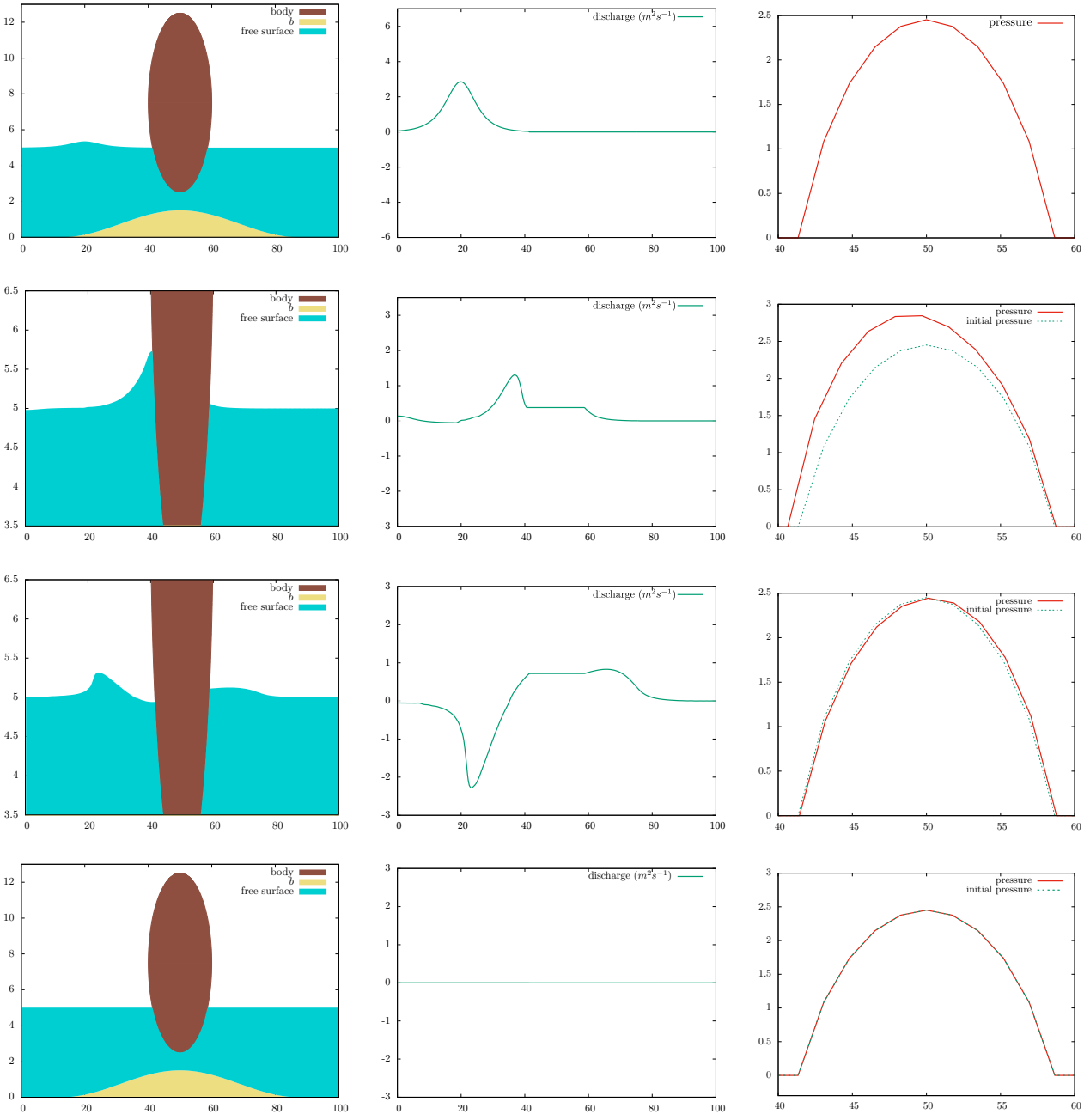

(a) Free-surface η^e (b) discharge q^e and q^i (c) inner pressure $\underline{p}_i/\rho g$

Figure 9: Test 3 - A solitary wave interacting with a partially immersed stationary object: surface elevation, discharge and inner pressure at the underside of the object for $n^e_{\text{el}} = 50$, $n^i_{\text{el}} = 10$ and $k = 3$.

4.4. A shock-wave interacting with a stationary object

In this fourth test-case, we consider a shock-wave propagating over a flat bottom, with a stationary partially immersed object located in the middle of the domain, in order to highlight the stabilization capabilities of the *a posteriori* LSC method in the vicinity of the object and emphasize the robustness of the resulting global DG-ALE formulation. We set $\Omega := [-20, 120]$, $n^e_{\text{el}} = 70$, $n^i_{\text{el}} = 10$ and $k = 3$.

h	$E^{\underline{\mathrm{p}}_{\mathrm{i}}}_{L_2}$
100/20	1.72E-3
100/50	8.07E-4
100/100	1.25E-5
100/150	4.40E-6
100/200	1.33E-7

Table 1: Test 3 - A solitary wave interacting with a partially immersed stationary object: L^2-errors between numerical and exact solution for the inner pressure $\underline{\mathrm{p}}_{\mathrm{i}}$, for $k = 3$ at time $T_{\max} = 100\,s$.

The initial data is defined as follows:

$$\eta_0^e(x) := \begin{cases} 6.5 & \text{if} \quad x \leq 0, \\ 5 & \text{elsewhere,} \end{cases}, \quad \eta_0^i := \mathrm{p}^k_{\mathscr{T}_h^{\mathrm{i},0}}(\eta_{\mathrm{lid}}), \qquad q_0^e := 0, \qquad q_0^i := 0.$$

Snapshots of the free-surface elevation at several time are shown on Fig. 10. We observe that the discontinuity, initially located in $\mathcal{E}_0^-$, propagates towards the object, generating some interesting nonlinear interactions. We emphasize that this configuration simultaneously involves a shock-wave propagation and reflection, displacement of the frame through the ALE description, a partial run-up over the surface-piercing object which is associated with the collision between the shock-wave and the object left-side and a partial transmission of the wave beyond the object with the formation of an interesting free-surface profile that looks like a rarefaction wave. This highlights the robustness of the global formulation and in particular the stabilization effect associated with the *a posteriori* LSC method . The dynamic of the free-boundaries is indeed computed in a very stable way, without any spurious oscillations or further time-step restriction. Additionally, a zoom on the free-surface discontinuity is displayed on Fig. 11, highlighting that the *a posteriori* LSC method is only activated in a very thin area in the vicinity of the propagating shock-wave.

4.5. Run-up of a solitary wave partially reflected by a stationary object

In this last test-case, we follow the propagation and run-up of a solitary wave over a plane beach, with a stationary partially immersed object placed on the way. The computational domain is set to $\Omega := [-200, 150]$, the topography is made of a constant depth area followed by a sloping beach of constant slope $1/11$. We set $k = 3$, $n^e_{\mathrm{el}} = 50$ and $n^i_{\mathrm{el}} = 10$. The initial data is defined as follows:

$$\eta_0^e(x) := H_0 + A_w \operatorname{sech}(\gamma(x - x_0)), \quad q_0^e := c_{q_2} \mathrm{g}(\eta_0^e - H_0) H_{e0}, \tag{94}$$

$$\eta_0^i(x) := \mathrm{p}^k_{\mathscr{T}_h^{\mathrm{i},0}}(\eta_{\mathrm{lid}}), \qquad q_0^i := 0.$$

with $A_w = 0.55\,m$, $x_0 = -80\,m$, $c_{q_1} = 0.1$, $c_{q_2} = 0.5$ and $\gamma := c_{q_1}\sqrt{\dfrac{3A_w}{4H_0}}$.

We show on Fig. 12 some snapshots of the free-surface elevation at several discrete times in the range $(1\,s,\, 300\,s)$. We observe a partial run-up and reflection of the wave on the object, while the remaining part of the wave is transmitted beyond the object, propagating further in $\mathcal{E}(t)$. This secondary wave subsequently reaches the shore, generating a run-up on the beach followed by a reflection. This reflected wave is itself again partially reflected by the object, generating a third sequence of run-up and reflection, while the transmitted wave propagates back in $\mathcal{E}^-(t)$ towards the

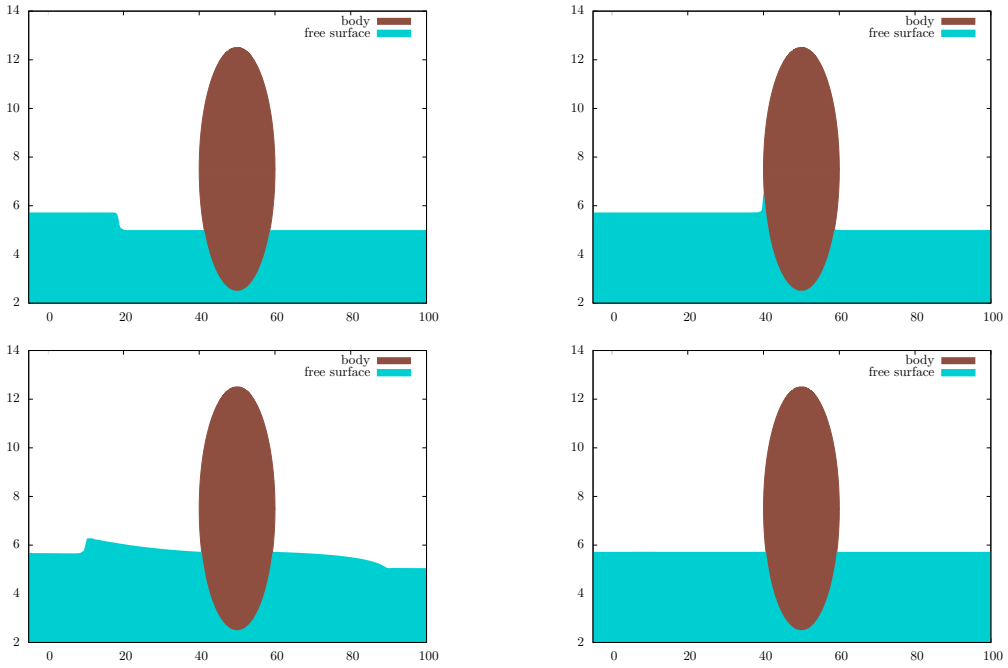

Figure 10: Test 4 - A shock-wave interacting with a stationary partially immersed object - Free-surface elevation computed at various times: $t = 2.7\,s$, $5.5\,s$, $14.8\,s$ and $44\,s$ with $k = 3$, $n_{\text{el}}^{e} = 70$ and $n_{\text{el}}^{i} = 10$.

domain's left boundary. In Fig. 13, we zoom on the shoreline area, highlighting the corrected and uncorrected sub-cells which are respectively plotted with green squares and blue dots. Again, we observe that the *a posteriori* LSC method is only activated in a very thin area in the vicinity of the wet/dry front. We also display on Fig. 14 a comparison between the maximum run-up observed with and without the embedded partially immersed object on place, in order to highlight the impact of the object presence on the run-up amplitude.

5. Conclusion

In this paper, we introduce a novel numerical approximation algorithm allowing to compute fluid-structure interactions between a partially immersed and stationary object in shallow water flows. This new discrete formulation is based on a DG-ALE global discretization for the flow model, coupled with a set of nonlinear ordinary differential equations for the resolution of the free-boundary problems associated with the time evolution of the air-fluid-structure interface, and the time evolution of the discharge beneath the object. In order to allow the computation of general waves interactions, possibly involving non-smooth surface waves, we extend the *a posteriori* LSC method of [14] to the current DG-ALE description. In particular, we show that the resulting global flow discrete formulation preserves the DGCL, as well as the well-balancing property for motionless steady states, for any order of approximation in space. The resulting numerical strategy combines the high accuracy of DG approximations, with a robust stabilization process which ensures the positivity of the water height at the sub-cell level, as well as preventing from the occurrence of spurious oscillations in the vicinity of discontinuities, discontinuities of the gradient and extrema. More general configurations involving moving floating objects are currently investigated and will be studied in future works.

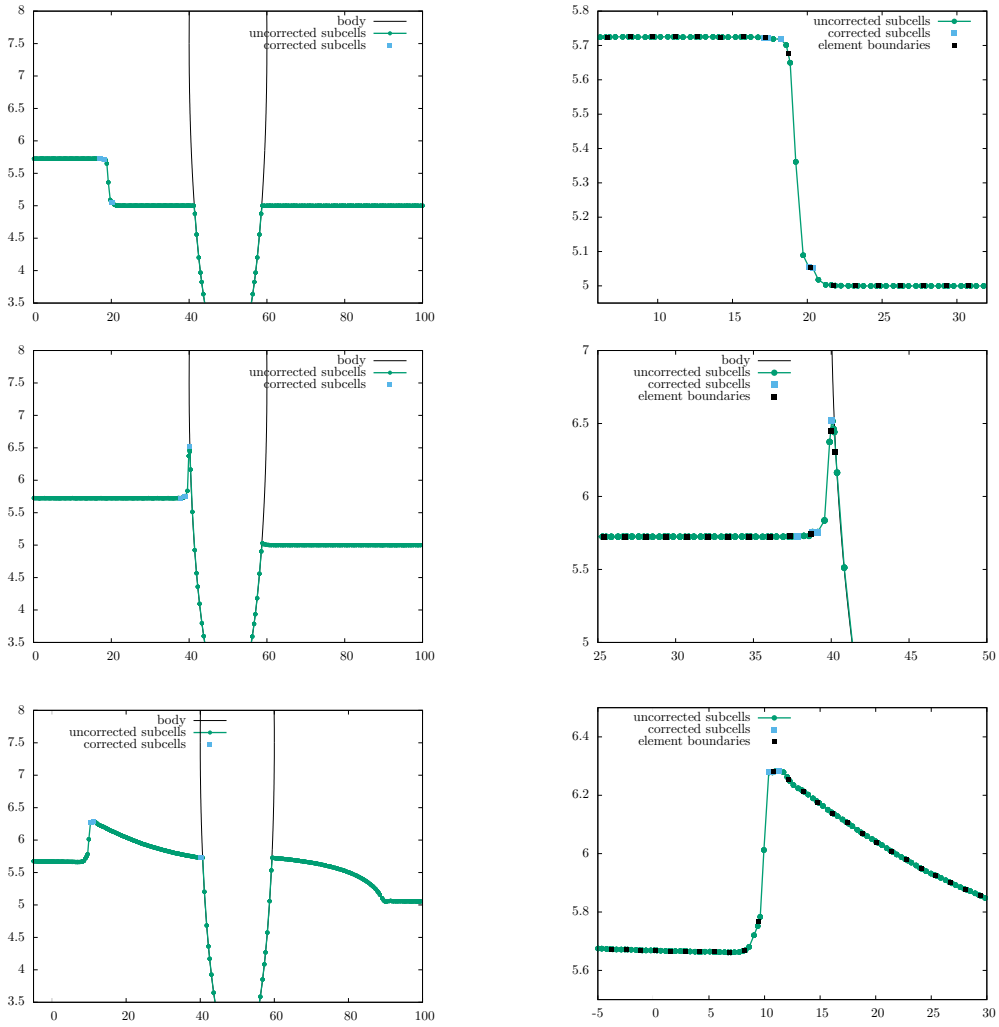

Figure 11: Test 4 - A shock-wave interacting with a stationary partially immersed object - Free-surface elevation computed for different values of time $t = 2.7\,s$, $5.5\,s$ and $14.8\,s$. The corrected and uncorrected sub-cells are respectively plotted with blue squares and green dots, with a zoom on the discontinuity, for $k = 3$, $n_{\text{el}}^e = 70$ and $n_{\text{el}}^i = 10$.

Acknowledgment

F. Marche gratefully acknowledges the support provided under Agence Nationale de la Recherche (ANR) project NABUCO (ANR-17-CE40-0025).

Appendix A. Cut-off function

The cut-off function $\varphi \in \mathcal{D}(\mathbb{R})$ used in (28) is defined as follows:

$$\forall x \in \mathbb{R}, \quad \varphi(x) := e\,\psi_e(\varepsilon_0 x),$$

where

$$\forall x \in \mathbb{R}, \quad \psi_e(x) := \phi_e(1 - |x|^2),$$

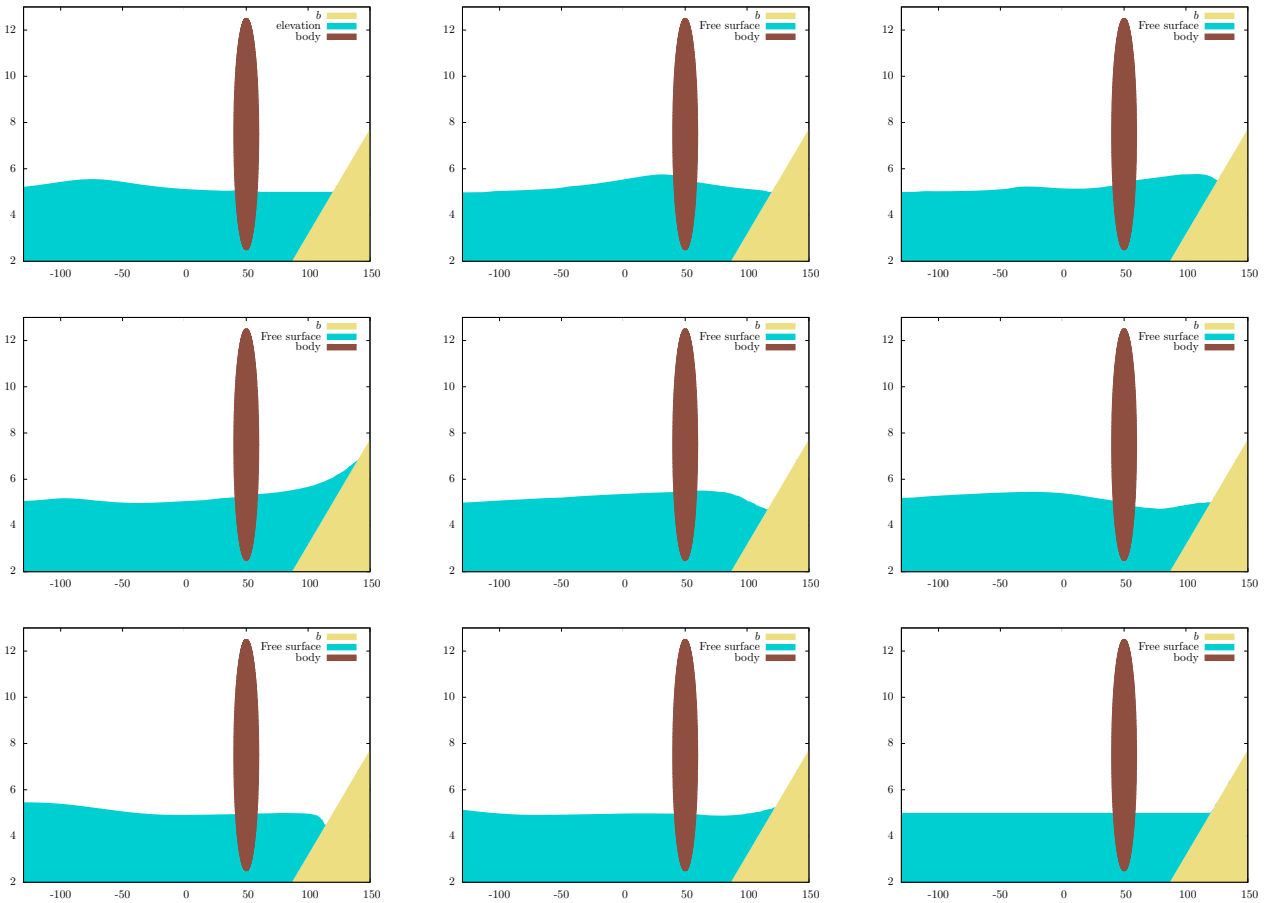

Figure 12: Test 5 - Run-up of a solitary wave partially reflected by a stationary object - Free-surface obtained at several times in the range $[1\,s,\ 300\,s]$, with $k = 3$ and $n^e_{\text{el}} = 50$, $n^i_{\text{el}} = 10$.

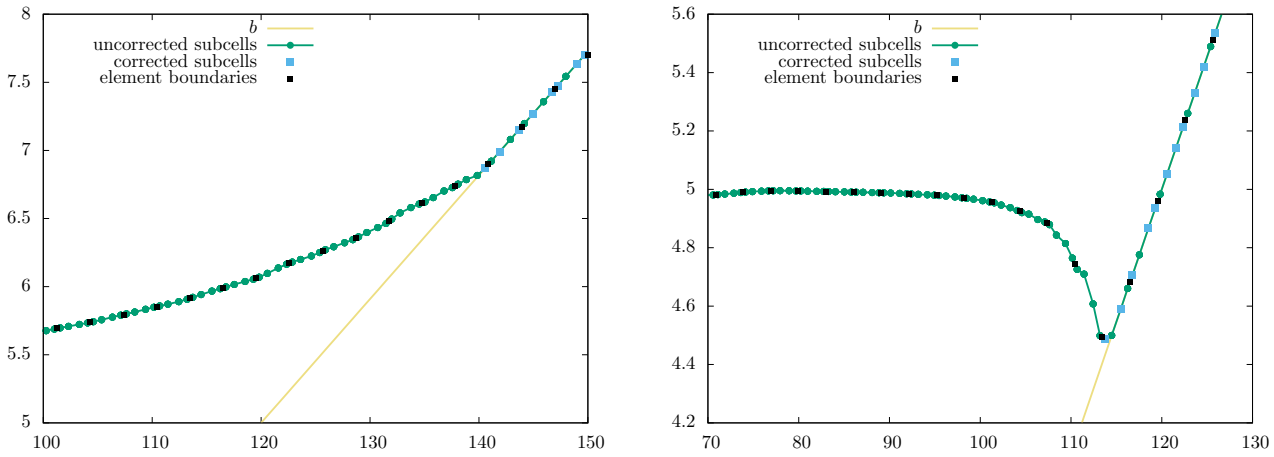

Figure 13: Test 5 - Run-up of a solitary wave partially reflected by a stationary object - Zoom on the shoreline showing the free-surface at $t = 35\,s$ (left) and $t = 69\,s$ (right), with corrected and uncorrected sub-cells respectively plotted with blue squares and green dots, for $k = 3$ and $n^e_{\text{el}} = 50$, $n^i_{\text{el}} = 10$.

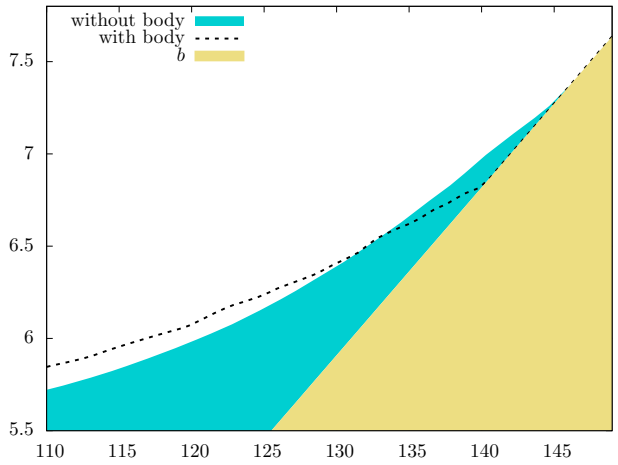

Figure 14: Test 5 - Run-up of a solitary wave partially reflected by a stationary object - Snapshot of the free-surface corresponding to the maximum run-up observed with the embedded partly immersed object (in dashed-line) and without the object (in blue).

and

$$\forall t \in \mathbb{R}, \quad \phi_e(t) := \begin{cases} e^{-t^{-1}} & \text{if} \quad t > 0 \\ \\ 0 & \text{elsewhere,} \end{cases}$$

Note that we have $\text{supp}(\psi_e) \subset \overline{B}(0,1)$, $\text{supp}(\varphi) \subset [-\frac{1}{\varepsilon_0}, \frac{1}{\varepsilon_0}]$ and ε_0 chosen such that we have $\varphi(x) = 1$, $\forall |x| \leq 1$.

Appendix B. Definition of the elliptic object

In this work, we consider a partially immersed object $\mathcal{O}_{\text{bj}}$, which center of mass is located at $(x_{\text{G}}, z_{\text{G}})$ and which boundary is denoted by $\partial\mathcal{O}_{\text{bj}}$. Denoted respectively by a, b its major and minor radius, we define $\partial\mathcal{O}_{\text{bj}}$ as an ellipse, so that we have:

$$(x, y) \in \partial\mathcal{O}_{\text{bj}} \quad \Longleftrightarrow \quad \frac{(x - x_{\text{G}})^2}{a^2} + \frac{(z - z_{\text{G}})^2}{b^2} = 1.$$

The underside of the object may be locally parameterized as follows:

$$\forall x \in \mathcal{I}_{\text{lid}} := [x_{\text{G}} - a, x_{\text{G}} + a], \quad \eta_{\text{lid}}(x) := z_{\text{G}} - b\sqrt{1 - \frac{(x - x_{\text{G}})^2}{a^2}}.$$

Note that denoting $z_{\text{G}} = H_0 + e_0$, we have:

$$X_0^{\pm} := x_{\text{G}} \pm \sqrt{a^2 - \frac{a^2 {e_0}^2}{b^2}}.$$

References

[1] L. Arpia and M. Ricchiuto. Well balanced residual distribution for the ALE spherical shallow water equations on moving adaptive meshes. *J. Comput. Phys.*, 405:109–173, 2019.

[2] U. Bosi, A.P. Engsig-Karup, C. Eskilsson, and M. Ricchiuto. A spectral/hp element depth-integrated model for nonlinear wave–body interaction. *Comp. Meth. App. Mech. Eng.*, 348:22–249, 2019.

[3] Q. Chen and I. Babuska. Approximate optimal points for polynomial interpolation of real functions in an interval and in a triangle. *Comput. Methods Appl. Mech. Engrg*, 128:405–417, 1995.

[4] X.N. Chen and S.D. Sharma. A slender ship moving at a near-critical speed in a shallow channel. *J. Fluid Mech.*, 291:263–285, 1995.

[5] B. Cockburn and C.-W. Shu. Runge-Kutta Discontinuous Galerkin methods for convection-dominated problems. *J. Sci. Comput.*, 16(3):173–260, 2001.

[6] A.J.-C. de Saint-Venant. Théorie du mouvement non-permanent des eaux, avec application aux crues des rivières et à l'introduction des marées dans leur lit. *C.R. Acad. Sci. Paris, Section Mécanique*, 73:147–154, 1871.

[7] J. Donea, A. Huerta, J.-Ph. Ponthot, and A. Rodríguez-Ferran. *Arbitrary Lagrangian–Eulerian Methods, The Encyclopedia of Computational Mechanics*, pages 413–437. Wiley, 2004.

[8] A. Duran and F. Marche. Recent advances on the discontinuous Galerkin method for shallow water equations with topography source terms. *Comput. Fluids*, 101:88–104, 2014.

[9] E. Godlewski, M. Parisot, J. Sainte-Marie, and F. Wahl. Congested shallow water model: roof modelling in free surface flow. *ESAIM Math. Model. Numer. Anal.*, 52(5):1679 – 1707, 2018.

[10] E. Godlewski, M. Parisot, J. Sainte-Marie, and F. Wahl. Congested shallow water model: on floating body. *SMAI Journal of Computational Mathematics*, in press, 2022.

[11] S. Gottlieb, C.-W. Shu, and Tadmor E. Strong stability preserving high order time discretization methods. *SIAM Review*, 43:89–112, 2001.

[12] H. Guillard and C. Farhat. On the significance of the geometric conservation law for flow computations on moving meshes. *Comput. Methods Appl. Engrg*, 190:1467–1482, 2000.

[13] C. Hague and C. Swan. A multiple flux boundary element method applied to the description of surface water waves. *J. Comput. Phys.*, 228(14):5111–5128, 2009.

[14] A. Haidar, F. Marche, and F. Vilar. A posteriori finite-volume local subcell correction of high-order discontinuous Galerkin schemes for the nonlinear shallow-water equations. *J. Comput. Phys.*, 452:110902, 2022.

[15] C.W. Hirt, A.A. Amsden, and J.L. Cook. An arbitrary lagrangian–eulerian computing method for all flow speed. *J. Comput. Phys.*, 135:203–216, 1997.

[16] T. Iguchi and D. Lannes. Hyperbolic free boundary problems and applications to wave-structure interactions. *Indiana Univ. Math. J.*, 70:353–464, 2021.

[17] T. Jiang. *Ship Waves in Shallow Water*. Verkehrstechnik, Fahrzeugtechnik. Fortschritt-Berichte VDIReihe, 2001.

[18] T. Jiang, R. Henn, and S.D. Sharma. Wash waves generated by ships moving on fairways of varying topography. In *24th Symposium on Naval Hydrodynamics Fukuoka, JAPAN*, 2002.

[19] F. John. On the motion of floating bodies i. *Communications on Pure and Applied Mathematics*, 2:13–57, 1949.

[20] E.V. Koutandos, T.V. Karambas, and C.G. Koutitas. Floating breakwater response to waves action using a boussinesq model coupled with a 2dv elliptic solver. *J. Waterw. Port Coastal Ocean Eng.*, 130:243–255, 2004.

[21] E.E. Kriezi, T. Karambas, P. Prinos, and C. Koutitas. Interaction of floating breakwaters with waves in shallow waters. In *Proc., Int. Conf. IAHR, Beijing*, 2001.

[22] D. Lannes. On the dynamics of floating structures. *Annals of PDE*, 2017.

[23] C. Lee and J.N. Newman. Computation of wave effects using the panel method. In *Numerical Models in Fluid-Structure Interaction*, 2005.

[24] Q. Liang and F. Marche. Numerical resolution of well-balanced shallow water equations with complex source terms. *Advances in Water Resources*, 32(6):873 – 884, 2009.

[25] I. Lomtev, R.M. Kirby, and G.E. Karniadakis. A discontinuous Galerkin ALE method for compressible viscous flows in moving domains. *J. Comput. Phys.*, 155(1):128–159, 1999.

[26] T.F. Ogilvie. Second-order hydrodynamic effects on ocean platforms. In *Proc. Intl. Workshop on Ship and Platform Motions, ed. R. W. Yeung, University of California, Berkeley*, pages 205–265, 1983.

[27] P.-O. Persson, J. Peraire, and J. Bonet. Discontinuous Galerkin solution of the Navier–Stokes equations on deformable domains. *Comp. Meth. App. Mech. Eng.*, 198:1585–1595, 2009.

[28] C.-W. Shu and S. Osher. Efficient implementation of Essentially Non-Oscillatory shock-capturing schemes. *J. Comput. Phys.*, 77:439–471, 1988.

[29] P.D. Thomas and C.K. Lombard. Geometric conservation law and its applications to flow computations on moving grids. *AIAA Journal*, 17:1030–1037., 1979.

[30] J.J.W. van de Vegt and Y. Xu. Space-time discontinuous galerkin method for nonlinear water waves. *J. Comput. Phys.*, 224:17–39, 2007.

[31] J.J.W. Van der Vegt and H. Van der Ven. Space-time discontinuous Galerkin finite element method with dynamic grid motion for inviscid compressible flows. *J. Comput. Phys.*, 182:546–585, 2002.

[32] C.S. Ventakasubban. A new finite element formulation for ALE (arbitrary Lagrangian Eulerian) compressible fluid mechanics. *Int. J. Engrg. Sci.*, 33:1743–1762, 1995.

[33] F. Vilar. A posteriori correction of high-order discontinuous galerkin scheme through subcell finite volume formulation and flux reconstruction. *J. Comput. Phys.*, 387:245–279, 2019.

[34] A. N. Williams and W. G. McDougal. Flexible floating break-water. *J. Waterw. Port Coastal Ocean Eng.*, 117(5):429–450, 1991.

[35] G.Q. Yang, O.M. Faltinsen, and R. Zhao. Wash of ships in finite water depth. In *Proceedings of the FAST 2001, Southhampton, UK*, 2001.

[36] Y.H. Yu and L. Ye. Reynolds-averaged navier stokes simulation of the heave performance of a two-body floating-point absorber wave energy system. *Computers and Fluids*, 73:104–114, 2013.